Article:
Altalhi, N.R., Lesnic, D. and Griffiths, S.D. (Accepted: 2026) Determination of boundary corrosion characteristics using the boundary element method. Engineering Analysis with Boundary Elements. ISSN: 0955-7997 (In Press)

Determination of boundary corrosion characteristics using the boundary element method

N.R. Altalhi[1,2], D. Lesnic[1,*] and S.D. Griffiths[1]

[1] *Department of Applied Mathematics, University of Leeds, Leeds LS2 9JT, UK*
[2] *Department of Mathematics, University of Taif, Taif, Saudi Arabia*
[*] Corresponding author (D.Lesnic@leeds.ac.uk)

Abstract

During their lifetime, engineering systems, such as buried pipelines, rooftops, chemical plants and off-shore structures, are exposed to hostile extreme environments leading to inherent corrosion attacks. These can compromise their structural integrity and pose significant risks to the environment and public safety, let alone the huge economic loss due to corrosion. Therefore, monitoring and detecting corrosion using inverse modelling is paramount. In this paper, inverse problems arising in corrosion detection are investigated. Such problems concern determining the corroded portion of the boundary of a specimen, e.g., a pipe or ship hull placed in a corrosive environment, and possibly its associated coefficient of corrosion from one or two pairs of Cauchy data (boundary potential and current flux) measurements taken on a part of the uncorroded boundary. We develop the boundary element method (BEM) to establish boundary integral equations that relate the boundary data to the unknown corrosion characteristics. Then, we minimize iteratively the difference between the measured and computed potential on the accessible boundary where measurements are taken. Furthermore, since the inverse problems under investigation are ill-posed, the objective least-squares functional is regularised through the inclusion of a penalty term aimed to improve the stability of solution. The accuracy and stability of the developed numerical BEM constrained minimization algorithm are investigated with respect to noise in the input measured data and various regularization parameters.

Keywords: Boundary element method; boundary corrosion detection; coefficient of corrosion; inverse problems

1 Introduction

In an age when engineering systems and materials are continuously re-designed and improved to withstand ever increasing hostile, aggressive and extreme environments, modelling corrosion remains of utmost importance. Within this framework, determining (monitoring and detecting) the boundary characteristics are essential to reduce the huge economic loss due to corrosion of engineering systems encountered in rooftops [27], blast furnace hearths [114], coolant flow passages in wings and turbine blades [68, 86],

underground pipes, chemical plants, ship hulls and off-shore structures [14, 106, 117]. To understand the corrosion of such structures, one needs to analyse the current flux and electrical potential data over the boundary. Specifically, when a material Ω is subjected to a corrosion attack, the damaged boundary $\Gamma_0 \subset \partial\Omega$ is subjected to a Robin boundary condition (see later on equation (2.3)) linking the flux with the potential through a corrosion coefficient λ.

Many theoretical and numerical studies have considered the separate retrieval (in terms of aspects related to uniqueness, stability and numerical reconstruction) of the unknown corroded boundary Γ_0 (insulated for $\lambda = 0$ or perfectly conductive for $\lambda = \infty$), see [18, 46, 67, 69], or of the unknown corrosion coefficient λ (when Γ_0 is known) in the case of linear corrosion, see equation (3.1), see [61, 62, 75, 76], from a single pair of the boundary Cauchy data measurements on $\Gamma = \partial\Omega\backslash\Gamma_0$. The simultaneous recovery of both the boundary Γ_0 and the corrosion coefficient λ was much less addressed [29, 72, 105].

1.1 Novelty of the paper

The novelty of the paper is to formulate and investigate three new inverse problems, in increasing order of difficulty, for the more realistic case when the law of boundary corrosion is nonlinear. For each of these problems, discussion and comparison with the much more investigated linear law of corrosion case cited above, are undertaken. Furthermore, since all the unknowns are associated with the boundary only, the BEM is developed as the most natural and reliable numerical method of discretising the governing Laplace's equation subjected to linear and nonlinear boundary conditions. Then, the resulting boundary integral formulations are made applicable for inverse analysis by minimising, with respect to the unknown corrosion characteristics, the difference between the measured and computed boundary potential augmented with regularization terms to achieve stable reconstructions.

1.2 Plan of the paper

The plan of the paper is as follows. Section 2 formulates mathematically the direct and inverse corrosion problems under investigation. Problem analyses for the cases of linear and nonlinear laws of corrosion are detailed in sections 3 and 4, respectively. The physical scenario related to an underground corroded pipe is mathematically modelled in section 5. Sections 6 and 7 develop the boundary element method (BEM) and the method of the fundamental solutions (MFS), respectively, for the discretisation or approximation of the electric potential satisfying the Laplace's equation. Possible current flux inputs are discussed in section 8. Numerical results for the direct and inverse problems I–III are presented and discussed in sections 9–12, respectively. Finally, section 13 highlights the conclusions of the study, including insights, recommendations, extensions and limitations, and suggests some possible directions for future work.

2 Mathematical formulations

Let $\Omega \subset \mathbb{R}^d$ (of dimension $d = 2$ or 3) be a bounded connected domain with sufficiently smooth boundary, say $\partial\Omega \in C^{2,\beta}$, where $C^{k,\beta}$ denotes the set of k–times Hölder continuously differentiable functions with exponent $\beta \in (0, 1)$. Let the boundary $\partial\Omega$ be composed of the union of an uncorroded portion Γ and a corroded portion $\Gamma_0 = \partial\Omega\backslash\Gamma$.

When modelling the electrochemistry of corrosion, the electrode charge–transfer reactions at the interface between a specimen and its electrolytic environment lead to considering [116] the electrical potential u satisfying the Laplace equation

$$\nabla^2 u = 0 \quad \text{in } \Omega, \tag{2.1}$$

subject to the Neumann boundary condition

$$\frac{\partial u}{\partial n} = g \quad \text{on } \Gamma, \tag{2.2}$$

and the Robin-type boundary condition

$$\frac{\partial u}{\partial n} = \lambda f(u) \quad \text{on } \Gamma_0 = \partial\Omega \setminus \Gamma, \tag{2.3}$$

where $\underline{n}$ is the outward unit normal to $\partial\Omega$, λ denotes the coefficient of corrosion and $f(u)$ is the corrosion law - known also as the polarization response expressing the relationship between the current flux and the potential on the corroded boundary Γ_0. We note that if λ is a positive constant, and Γ and Γ_0 are disjoint then the direct nonlinear boundary value problem (2.1)–(2.3) has a unique solution $u \in C^{2,\alpha}(\overline{\Omega})$ for some $\alpha \in (0,1)$, in case $\Omega \subset \mathbb{R}^2$ is a bounded domain with boundary $\partial\Omega$ of class $C^{2,\alpha}$, $f \in \mathcal{F} := \{f \in C^{3,\alpha}(\mathbb{R}) | f' \leq 0\}$ and $0 \not\equiv g \in C^{3,\alpha}(\Gamma)$, see [48] and [63, Theorems 17.28 and 17.30]. Moreover, the mapping $\mathcal{F} \ni f \mapsto u_f \in C^{2,\alpha}(\overline{\Omega})$ is continuous when $\mathcal{F}$ is equipped with the topology of $C^{1,\alpha}$, see [48] and [63, Theorem 6.30]. The Neumann boundary condition (2.2) specifying the current flux g may be replaced by the Dirichlet boundary condition,

$$u = h \quad \text{on } \Gamma, \tag{2.4}$$

specifying the boundary potential h, see [118]. In the boundary condition (2.3) modelling the damage due to corrosion, the resistivity coefficient of corrosion λ represents the reciprocal of the impedance and the law of corrosion is given by

$$f(u) = u_a - u \quad \text{for the linear Newton's law of convection,} \tag{2.5}$$

where u_a is the ambient potential, or, if we take into account the chemical reduction and oxidation which occur on the corroded boundary Γ_0, see [116],

$$f(u) = -2\sinh\left(\frac{u}{2}\right) \quad \text{for the nonlinear Butler-Volmer law of polarization.} \tag{2.6}$$

In case the polarization curve $f(u)$ expressing the relationship between the current flux $\partial u/\partial n$ and the potential u on the corroded boundary Γ_0 is not available, one can estimate it from the potential values measured on a portion of the accessible boundary Γ far from Γ_0, see the inverse analyses of [14, 15] for estimating the galvanic corrosion and [4, 5, 102, 112] for more general corrosion law identifications. Various algorithms for corrosion detection problems associated with the electrostatic model (2.1)–(2.6) were considered and reviewed in [10, 11], which also include other models of corrosion detection based on guided waves [12] or ultrasound [13].

As mentioned above in subsection 1.1, in this paper, we consider three inverse corrosion problems formulated in increasing order of difficulty. In these settings, Γ is known and accessible for input/output Cauchy data measurements, whilst Γ_0 has unknown characteristics and is inaccessible to direct measurement (perhaps Γ_0 is some interior connected

component of $\partial\Omega$, as in the cavity or rigid inclusion determination [9], or some corroded portion of the exterior component of $\partial\Omega$, see [87]).

Inverse problem I (identification of the corrosion coefficient λ).
In case the space-dependent corrosion coefficient λ in (2.3) is unknown, the inverse boundary coefficient problem requires finding the solution pair (u, λ) satisfying (2.1)–(2.3) and the additional measurement of the potential u on a sub-portion Γ_2 of Γ given by

$$u = h \quad \text{on } \Gamma_2. \tag{2.7}$$

Essentially, the same inverse problem arises in steady heat conduction where λ signifies the heat transfer coefficient and u represents the temperature [115].

Inverse problem II (identification of the corroded boundary Γ_0).
In case the corroded boundary Γ_0 in (2.3) is unknown, the inverse boundary determination problem requires finding the solution pair (u, Γ_0) satisfying (2.1)–(2.3) and (2.7). Essentially, the same inverse boundary problem arises when monitoring the unknown wear-line of a melting furnace [113]. The measurement (2.7) may be recorded more than once, as generated by different (functionally independent) current fluxes imposed in (2.2). For example, for two current fluxes $g^{(1)}$ and $g^{(2)}$ imposed on Γ as

$$\frac{\partial u}{\partial n} = g^{(i)} \quad \text{on } \Gamma, \tag{2.8}$$

we measure the potential

$$u = h^{(i)} \quad \text{on } \Gamma_2, \tag{2.9}$$

for $i = 1, 2$.

Inverse problem III (identification of the corrosion coefficient λ and the corroded boundary Γ_0).
In case that both the space–dependent corrosion coefficient λ and the corroded boundary Γ_0 are unknown in (2.3), a combination of the inverse problems I and II requires finding the triplet (u, λ, Γ_0) satisfying (2.1)–(2.3) and (2.7), where the measurement of (2.7) may be recorded more than once, as described in (2.8) and (2.9). This class of inverse problem is most challenging due to the intrinsic coupling between the unknown geometry and material parameters [29, 59, 101]. Similar inverse problems, in acse of the linear corrosion law (2.5), were investigated using the MFS in [20, 81].

In the next sections 3 and 4 we analyse in more detail the direct and inverse problems in case of the linear and nonlinear boundary corrosion laws (2.5) and (2.6), respectively.

3 Analysis of linear corrosion

Taking for simplicity, $u_a = 0$ in (2.5), the resulting linear boundary corrosion law, which also arises as a linearisation of the Butler–Volmer nonlinear law (2.6), see [108], recasts equation (2.3) as

$$\frac{\partial u}{\partial n} + \lambda u = 0 \quad \text{on } \Gamma_0. \tag{3.1}$$

Other derivations of (3.1) based on the Faraday's law of electrochemical corrosion [78], or on modelling the corroded boundary Γ_0 as a thin irregular coating layer can be found in [28, 87, 88].

3.1 The direct linear problem given by equations (2.1), (2.2) and (3.1)

It is known, see e.g., [63], that if $\partial\Omega \in C^{2,\beta}$, $0 \leq \lambda \in C^{1,\beta}(\Gamma_0)$, $\lambda \not\equiv 0$ and $g \in H^{-1/2}(\Gamma)$ (or $C^{1,\beta}(\Gamma)$), then the Neumann–Robin direct problem (2.1), (2.2) and (3.1) has a unique solution $u \in H^1(\Omega)$ (or $C^{2,\beta}(\Omega)$). A similar unique solvability result holds for the Dirichlet–Robin direct problem (2.1), (2.4) and (2.7) if $h \in H^{1/2}(\Gamma)$ (or $C^{2,\beta}(\Gamma)$).

3.2 The inverse problem I given by equations (2.1), (2.2), (2.7) and (3.1) for the determination of the coefficient of corrosion

If the prescribed current flux in (2.2) satisfies $0 \not\equiv g \in H^{-1/2}(\Gamma)$, then the measurement (2.7) of the potential on Γ_2 suffices to determine uniquely the corrosion coefficient λ in the class of admissible function

$$\Lambda^1_{a,d} := \left\{ \lambda \in C(\overline{\Gamma}_0) \middle| \ 0 < \min \lambda\big|_{\overline{\Gamma}_0} \right\} \tag{3.2}$$

together with the potential $u \in H^1(\Omega)$ satisfying the inverse problem I given by equations (2.1), (2.2), (2.7) and (3.1), see [32]. The positivity of λ in (3.2) is needed to ensure that a solution to the linear direct problem given by equations (2.1), (2.2) and (3.1) with known λ is unique. Indeed, if $\lambda \in \Lambda^1_{ad}$ then, multiplying by u equation (2.1) and using (2.2) and (3.1), the resulting identity

$$\int_\Omega |\nabla u|^2 \, d\Omega = \int_\Gamma gu \, d\Gamma - \int_{\Gamma_0} \lambda u^2 \, d\Gamma_0,$$

yields the uniqueness of solution $u \in H^1(\Omega)$ of the direct linear problem (2.1), (2.2) and (3.1). The unique identifiability of the corrosion coefficient λ also holds in the admissible class [71],

$$\Lambda^2_{ad} := \left\{ \lambda \in C^3_0(\overline{\Gamma}_0) \middle| \ 0 \not\equiv \lambda \geq 0 \right\} \tag{3.3}$$

and even in the more general class [33],

$$\Lambda_{ad} := \left\{ \lambda \in C(\overline{\Gamma}_0) \middle| \ 0 \not\equiv \lambda \geq 0 \right\} \supset \Lambda^1_{ad} \cup \Lambda^2_{ad}. \tag{3.4}$$

Various logarithmic stability estimates for inverse corrosion coefficient problems were obtained in [3, 34, 48, 49]. Moreover, if λ is sought as a piecewise constant function, Lipschitz stability estimates (with the Lipschitz constant increasing with the number of portions) are also possible [111]. Hölder stability estimates also hold in particular cases, e.g., if Γ_0 is a line segment or a part of some circle and λ is analytic or piecewise constant function, see [66] or, for other special cases, [97].

3.3 The inverse problem II given by equations (2.1), (2.2), (2.7) and (3.1) for the determination of the corroded boundary

The uniqueness of solution of the inverse problem II given by equations (2.1) and (3.1) in the case of a single Cauchy data pair measurements (2.2) and (2.7) is not guaranteed, unless $\lambda = 0$ or $\lambda = \infty$ in (3.1), see e.g., [18, 29, 46, 73]. Here we can also mention the related corrosion situation in which Ω is an annular domain with disjoint sub-boundaries Γ and Γ_0 and the interest is to non-destructively detect the boundary Γ_0 enclosing a

cavity, in case $\lambda = 0$, or a rigid inclusion, in case $\lambda = \infty$, see [2, 90, 92, 104] and [23, 39, 55, 84, 85] for theory and numerical reconstruction algorithms, respectively. In the case $0 < \lambda < \infty$, the unique determination of Γ_0 from a single Cauchy data pair does not hold in general [29], although local uniqueness may hold in the particular case that Ω is a thin rectangular plate [72]. The uniqueness in determining Γ_0 however is ensured if two functionally independent Cauchy data pairs given by equations (2.8) and (2.9) are provided [29].

3.4 The inverse problem III given by equations (2.1), (2.2), (2.7) and (3.1) for the determination of both the corroded boundary and the coefficient of corrosion

The unique simultaneous determination of both Γ_0 and λ from the two functionally independent Cauchy data pairs (2.8) and (2.9) is ensured if one of the Neumann data $g^{(1)}$ or $g^{(2)}$ or Dirichlet data $h^{(1)}$ or $h^{(2)}$ is positive [16, 103].

4 Analysis of nonlinear corrosion

In case the polarization response is given by the Butler–Volmer law (2.6), the nonlinear Robin boundary condition (2.3) recasts as

$$\frac{\partial u}{\partial n} + 2\lambda \sinh\left(\frac{u}{2}\right) = 0 \quad \text{on } \Gamma_0. \tag{4.1}$$

4.1 The direct nonlinear problem given by equations (2.1), (2.2) and (4.1)

Clearly, for $\lambda = 0$ the solution of the Neumann problem (2.1), (2.2) and $\partial u/\partial n = 0$ on Γ_0 is unique up to a constant (and it exists if $\int_\Gamma g \, d\Gamma = 0$). For $\lambda \in \Lambda_{ad}$, the direct nonlinear mixed problem (2.1), (2.2) and (4.1) has a unique solution characterised as the minimizer of the associated energy, see [25],

$$E(\mathrm{w}) = \frac{1}{2}\int_\Omega |\nabla \mathrm{w}|^2 \, d\Omega + \int_{\Gamma_0} \lambda F(\mathrm{w}) \, d\Gamma_0 - \int_\Gamma g\mathrm{w} \, d\Gamma, \quad \forall \mathrm{w} \in C^2(\Omega), \tag{4.2}$$

where $F(\mathrm{w}) = 4\cosh\left(\frac{\mathrm{w}}{2}\right)$. Indeed, let $v \in C^2(\Omega)$ be a test function. Denote $u_\epsilon = u + \epsilon v$ for ϵ small. Then the variation of the energy (4.2) is given by

$$\begin{aligned}
\frac{d}{d\epsilon}E(u_\epsilon)\Big|_{\epsilon=0} &= \frac{d}{d\epsilon}\left[\frac{1}{2}\int_\Omega |\nabla(u+\epsilon v)|^2 \, d\Omega + \int_{\Gamma_0} \lambda F(u+\epsilon v) \, d\Gamma_0 - \int_\Gamma (u+\epsilon v) g \, d\Gamma\right]_{\epsilon=0} \\
&= \int_\Omega \nabla u \cdot \nabla v \, d\Omega + \int_{\Gamma_0} \lambda F'(u) v \, d\Gamma_0 - \int_\Gamma v g \, d\Gamma \\
&= -\int_\Omega v\,(\nabla^2 u) \, d\Omega + \int_{\partial\Omega} v \frac{\partial u}{\partial n} \, d\Gamma + 2\int_{\Gamma_0} \lambda \sinh\left(\frac{u}{2}\right) v \, d\Gamma_0 - \int_\Gamma v g \, d\Gamma \\
&= -\int_\Omega v \, \nabla^2 u \, d\Omega + \int_{\Gamma_0} v \left(\frac{\partial u}{\partial n} + 2\lambda \sinh\left(\frac{u}{2}\right)\right) d\Gamma_0 + \int_\Gamma v \left(\frac{\partial u}{\partial n} - g\right) d\Gamma.
\end{aligned}$$

Setting the above variation equal to zero for any test function $v \in C^2(\Omega)$, we obtain that u satisfies the problem (2.1), (2.2) and (4.1).

Remark 4.1. *In case of the nonlinear corrosion boundary condition* (4.1) *there is yet no theoretical investigation into the uniqueness and stability of solution of the inverse problems I–III similar to those discussed in subsections 3.2–3.4 for the linear corrosion boundary condition* (3.1).

In the next section, we introduce the physical scenario of an underground pipe subjected to a corrosion attack.

5 Physical scenario

In the rest of the paper, we consider a physical scenario concerning the corrosion of a pipe buried in the ground. We assume that the pipe has cross-section a two-dimensional domain D that is star-shaped with respect to the origin and is embedded in a ground with a square cross-section, $[-L, L] \times [-L, L]$, with L say equal to 2. We assume also, that there is symmetry, for simplicity, such that we can consider the problem only in the first quadrant, i.e., the solution domain

$$\Omega = (0,2) \times (0,2) \backslash \left\{ r\big(\cos(\theta), \sin(\theta)\big) |\ \theta \in \left[0, \frac{\pi}{2}\right],\ 0 < r \leq r(\theta) < 2 \right\},$$

where $r(\theta)$ is the polar radius associated to the boundary ∂D. In this situation, the boundary $\partial\Omega$ of the solution domain Ω is formed from the union of the pieces $\big(\Gamma_i\big)_{i=\overline{0,4}}$, as depicted in Figure 1. On the boundaries Γ_1 and Γ_4 the flux g in equation (2.2) is zero due to the assumed symmetry, whilst the top boundary Γ_3 is assumed, for simplicity, to be insulated, so an adiabatic boundary condition is prescribed over it. On the corroded boundary $\Gamma_0 = \big\{ r(\theta)\big(\cos(\theta), \sin(\theta)\big) \big|\ \theta \in \big[0, \frac{\pi}{2}\big] \big\}$, the Robin boundary condition (2.3) applies, whilst on the right boundary Γ_2 $\big($away from $\Gamma_0\big)$ a current flux $g|_{\Gamma_2} \not\equiv 0$ is applied. In the inverse problems I–III, the resulting boundary potential $u|_{\Gamma_2} = h$ is measured, as given by (2.7). The above model, previously formulated in equations (2.1)–(2.3) and illustrated in Figure 1, becomes

$$\begin{cases} \nabla^2 u = 0 & \text{in } \Omega, \qquad (5.1) \\ \dfrac{\partial u}{\partial n} = \begin{cases} 0 & \text{on } \Gamma_1 \cup \Gamma_3 \cup \Gamma_4, \\ g \not\equiv 0 & \text{on } \Gamma_2, \end{cases} & \qquad (5.2) \\ \dfrac{\partial u}{\partial n} = \lambda(\theta)\, f(u) & \text{on } \Gamma_0, \qquad (5.3) \end{cases}$$

where the law of corrosion $f(u)$ is given by (2.5) or (2.6).

The next sections 6 and 7 develop two related but different numerical methods for solving the direct problem (5.1)–(5.3), with the obtained results presented and discussed in section 9 for the two imposed fluxes on Γ_2 defined in Section 8.

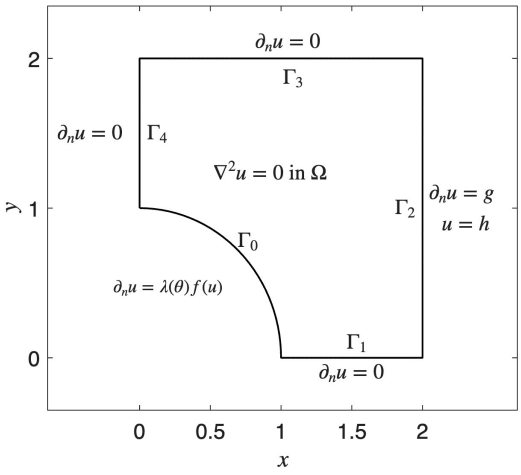

Figure 1: The geometry of the pipe corrosion problem and imposed boundary conditions.

6 The boundary element method for the direct problem (5.1)–(5.3)

As usual with the boundary element method (BEM), multiplying the Laplace's equation (5.1) by its two–dimensional fundamental solution $G(\underline{p};\underline{p}') = -\frac{1}{2\pi}\ln\left|\underline{p}-\underline{p}'\right|$, integrating using the Green's formula and applying the boundary conditions (5.2) and (5.3) yield the integral equation [7, 8]

$$\eta(\underline{p})u(\underline{p}) = \int_{\Gamma_0} G(\underline{p};\underline{p}')\lambda(\underline{p}')f\big(u(\underline{p}')\big)\,d\Gamma_0 + \int_{\Gamma_2} G(\underline{p};\underline{p}')g(\underline{p}')\,d\Gamma_2(\underline{p}') - \int_{\partial\Omega} u(\underline{p}')\frac{\partial G}{\partial n(\underline{p}')}(\underline{p};\underline{p}')\,dS(\underline{p}'), \quad \underline{p}\in\overline{\Omega}=\Omega\,\cup\,\partial\Omega, \quad (6.1)$$

where $\eta(\underline{p}) = 1$ if $p \in \Omega$ and $\eta(\underline{p}) = \frac{\chi(\underline{p})}{2\pi}$ if $p \in \partial\Omega$, and $\chi(\underline{p})$ is the angle formed by either tangents to $\partial\Omega$ at $\underline{p}$. In particular, if $\underline{p}$ is not a corner of $\partial\Omega$ then $\chi(\underline{p}) = \pi$ and thus $\eta(\underline{p}) = 1/2$. In three–dimensions, the fundamental solution changes to be $\frac{1}{4\pi|\underline{p}-\underline{p}'|}$.

We discretise the boundary $\partial\Omega$ in an anti-clockwise sense $\big($starting from the point $\underline{p}_0 = \big(0, r\big(\frac{\pi}{2}\big)\big) = (0,1) = \overline{\Gamma}_0\cap\overline{\Gamma}_4\big)$ using uniform divisions of the boundaries $\Gamma_0, \Gamma_1, \Gamma_2, \Gamma_3$ and Γ_4 into $N, N, 2N, 2N$ and N straight line segments, respectively, such that the mesh consists of a total of $7N = M$ boundary elements. Using a piecewise constant BEM approximation we assume that $u|_{\partial\Omega}, g|_{\Gamma_2}$ and $\lambda|_{\Gamma_0}$ are constant over each boundary element $[\underline{p}_{j-1}, \underline{p}_j]$ for $j = \overline{1, M}$ and take their values at the midpoint boundary element node $\tilde{p}_j = (\underline{p}_j + \underline{p}_{j-1})/2$, namely,

$$u(\underline{p}) \equiv u(\underline{\tilde{p}}_j) =: u_j \quad \text{for} \quad \underline{p}\in[\underline{p}_{j-1}, \underline{p}_j],\ j=\overline{1,M}, \quad (6.2a)$$

$$\lambda(\underline{p}) \equiv \lambda(\underline{\tilde{p}}_j) =: \lambda_j \quad \text{for} \quad \underline{p}\in[\underline{p}_{j-1}, \underline{p}_j],\ j=\overline{1,N}, \quad (6.2b)$$

$$g(\underline{p}) \equiv g(\underline{\tilde{p}}_j) =: g_j \quad \text{for} \quad \underline{p}\in[\underline{p}_{j-1}, \underline{p}_j],\ j=\overline{2N+1,4N}. \quad (6.2c)$$

With these approximations the equation (6.1) applied at each boundary element node $\tilde{p}_i$

for $i = \overline{1, M}$ is converted into the following system of M equations:

$$\sum_{j=1}^{N} A_{ij}\lambda_j f(\underline{u}_j) + \sum_{j=1}^{M} B_{ij}u_j = -\sum_{j=2N+1}^{4N} A_{ij}g_j, \qquad i = \overline{1, M}, \tag{6.3}$$

where

$$A_{ij} = \int_{[\underline{p}_{j-1}, \underline{p}_j]} G(\tilde{p}_i; \underline{p}')\, dS(\underline{p}'), \quad B_{ij} = -\int_{[\underline{p}_{j-1}, \underline{p}_j]} \frac{\partial G}{\partial n(\underline{p}')}(\tilde{p}_i; \underline{p}')\, dS(\underline{p}') - \frac{1}{2}\delta_{ij}, \quad i, j = \overline{1, M}, \tag{6.4}$$

and δ_{ij} is the Kronecker–delta symbol. The approximation of the boundary $\partial\Omega$ by the straight boundary element segments $[\underline{p}_{j-1}, \underline{p}_j]$ enables the analytical evaluation of the integrals in (6.4) in terms of the sides and angles of the typical BEM triangle formed with the vertices $\underline{p}$, $\underline{p}_{j-1}$ and $\underline{p}_j$; in particular, for any $\underline{p} \in \overline{\Omega}$ we have [94],

$$\begin{aligned} A_j(\underline{p}) &:= \int_{[\underline{p}_{j-1}, \underline{p}_j]} G(\underline{p}; \underline{p}')\, dS(\underline{p}') \\ &= -\frac{1}{2\pi} \begin{cases} h\big(\ln(h) - 1\big) & \text{if } ab = 0, \\ a\cos(\beta)\ln(a/b) - h(1 - \ln(b)) + a\,\psi\sin(\beta) & \text{if } ab \neq 0, \end{cases} \end{aligned} \tag{6.5}$$

$$\begin{aligned} B_j(\underline{p}) &:= \int_{[\underline{p}_{j-1}, \underline{p}_j]} \frac{\partial G}{\partial n(\underline{p}')}(\underline{p}; \underline{p}')\, dS(\underline{p}') \\ &= \begin{cases} 0 & \text{if } ab = 0 \text{ or } \underline{p} \in [\underline{p}_{j-1}, \underline{p}_j], \\ \psi\ \mathrm{sign}(\alpha_{j-1}(\underline{p}) - \alpha_j(\underline{p})) & \text{if } y \in [y_{j-1}, y_j], \\ \psi\ \mathrm{sign}(\alpha_j(\underline{p}) - \alpha_{j-1}(\underline{p})) & \text{otherwise}, \end{cases} \end{aligned} \tag{6.6}$$

where sign is the signum function, $a = |\underline{p} - \underline{p}_{j-1}|$, $b = |\underline{p} - \underline{p}_j|$, $h = |\underline{p}_j - \underline{p}_{j-1}|$,

$$\psi = \arccos\left(\frac{a^2 + b^2 - h^2}{2ab}\right), \quad \beta = \arccos\left(\frac{a^2 + h^2 - b^2}{2ah}\right),$$

and $\alpha_{j-1}(\underline{p}) \in [0, \pi]$ and $\alpha_j(\underline{p}) \in [0, \pi]$ are the angles between the positive x-axis and the straight lines $\overline{\underline{p}\underline{p}}_{j-1}$ and $\overline{\underline{p}\underline{p}}_j$ in the upper-half plane, respectively. The change in sign of the angle ψ in (6.6) occurs because the domain Ω is not convex. From (6.4)–(6.6) we observe that

$$A_{ij} = A_j(\underline{\tilde{p}}_i), \quad B_{ij} = -B_j(\underline{\tilde{p}}_i) - \frac{1}{2}\delta_{ij} \quad \text{for} \quad i, j = \overline{1, M}. \tag{6.7}$$

The system of nonlinear equations (6.3) is solved using the Matlab command `fsolve` to determine the Dirichlet boundary values u_j for $j = \overline{1, M}$. In case the boundary condition (2.3) linearizes as (3.1), the resulting system (6.3) becomes linear and given by

$$\sum_{j=1}^{N}(-A_{ij}\lambda_j + B_{ij})u_j + \sum_{j=N+1}^{M} B_{ij}u_j = -\sum_{j=2N+1}^{4N} A_{ij}\, g_j, \quad i = \overline{1, M}, \tag{6.8}$$

and is solved using the Matlab routine `linesolve`.

Since the direct problem (5.1)–(5.3) does not have an analytical solution available, it is useful to develop, as described in the next section, another independent method in order to compare the BEM results with and ensure that an accurate numerical solution has been obtained.

7 The method of fundamental solution for the direct problem (5.1)–(5.3)

A meshless approach, namely, the method of fundamental solution (MFS), see e.g. [77], may also be employed to solve the direct problem (5.1)–(5.3). The essential idea behind the MFS is to approximate the solution by a linear combination of non-singular fundamental solutions of the governing partial differential equation with reference to some sources located outside the solution domain [22]. Compared to the BEM based on boundary integral equations with source points located along the boundary, the MFS represents a straightforward discretization of a single-layer regular potential, which is permitted because the source points are positioned outside the closure of the solution domain, see [1, 26] for further comparisons between the BEM and the MFS.

In the MFS, we seek the solution to the Laplace equation (5.1) as a finite linear combination of fundamental solutions [45, 77],

$$u(\underline{p}) = \sum_{j=1}^{\mathcal{M}} C_j \, G(\underline{p}; \underline{\xi}_j), \quad \underline{p} \in \overline{\Omega}, \tag{7.1}$$

where $(\underline{\xi}_j)_{j=\overline{1,\mathcal{M}}}$ are source points (or 'singularities') selected outside $\overline{\Omega}$ and $(C_j)_{j=\overline{1,\mathcal{M}}}$ are unknown real coefficients to be determined by imposing the boundary conditions (5.2) and (5.3). Since $\underline{\xi}_j \notin \overline{\Omega}$ for $j = \overline{1,\mathcal{M}}$, the right-hand side of (7.1) represents a linear combination of harmonic functions in Ω, whose span is dense in the set of harmonic functions in Ω, see [22]. Based on the explicit representation (7.1), collocating the boundary conditions (5.2) and (5.3) at the nodes $(\tilde{\underline{p}}_i)_{i=\overline{1,M}}$ results in

$$\sum_{j=1}^{\mathcal{M}} C_j \, \frac{\partial G}{\partial n(\underline{p})}(\tilde{\underline{p}}_i, \underline{\xi}_j) = \lambda_i f \left(\sum_{j=1}^{M} C_j \, G(\tilde{\underline{p}}_i, \underline{\xi}_j) \right), \quad i = \overline{1,N}, \tag{7.2}$$

$$\sum_{j=1}^{\mathcal{M}} C_j \, \frac{\partial G}{\partial n(\underline{p})}(\tilde{\underline{p}}_i, \underline{\xi}_j) = \begin{cases} 0, & i = \overline{N+1,2N} \cup \overline{4N+1,M}, \\ g_i, & i = \overline{2N+1,4N}, \end{cases} \tag{7.3}$$

where

$$\frac{\partial G}{\partial n(\underline{p})}(\tilde{\underline{p}}_i, \underline{\xi}_j) = \nabla_{\underline{p}} G(\tilde{\underline{p}}_i, \underline{\xi}_j) \cdot \underline{n}(\tilde{\underline{p}}_i) = \frac{\partial G}{\partial x}(\tilde{\underline{p}}_i, \underline{\xi}_j) n_x(\tilde{\underline{p}}_i) + \frac{\partial G}{\partial y}(\tilde{\underline{p}}_i, \underline{\xi}_j) n_y(\tilde{\underline{p}}_i),$$

and $\tilde{\underline{p}}_i = (\tilde{x}_i, \tilde{y}_i)$, $\underline{\xi}_j = (\zeta_j, \eta_j)$, $\underline{n} = (n_x, n_y)$,

$$\frac{\partial G}{\partial x}(\tilde{\underline{p}}_i; \underline{\xi}_j) = -\frac{1}{2\pi} \frac{(\tilde{x}_i - \zeta_j)}{|\tilde{\underline{p}}_i - \underline{\xi}_j|^2}, \quad \frac{\partial G}{\partial y}(\tilde{\underline{p}}_i; \underline{\xi}_j) = -\frac{1}{2\pi} \frac{(\tilde{y}_i - \eta_j)}{|\tilde{\underline{p}}_i - \underline{\xi}_j|^2}.$$

Similar expressions employing the MFS for solving three-dimensional inverse geometric problems are also available [80, 99].

In case of the linear boundary (3.1) (in place of (5.3)), equations (7.2) simplify as

$$\sum_{j=1}^{\mathcal{M}} C_j \left[\frac{\partial G}{\partial n(\underline{p})}(\underline{\tilde{p}}_i; \underline{\xi}_j) + \lambda_i \, G(\underline{\tilde{p}}_i; \underline{\xi}_j) \right] = 0, \quad i = \overline{1, N}. \tag{7.4}$$

The source points $(\underline{\xi}_j)_{j=\overline{1,\mathcal{M}}}$ are placed on a dilated boundary at a constant distance $\delta > 0$ from $\partial\Omega$. There are several ways for choosing a suitable value for δ, as discussed in [42, 43], but herein we only mention that it depends on how far the harmonic solution of the direct problem (5.1)–(5.3) can be analytically continued in the exterior of Ω, see [100]. We also note that the ill-conditioning of the MFS system of equations (7.3) and (7.4) grows as the distance δ increases [41].

8 Imposed flux on Γ_2

As considered in [116], in the physical application, on the vertical wall Γ_2 we impose a current flux over an electrode of length 2ϵ centred at the point $(2, \frac{1}{3})$, which is drawn out through another electrode of length 2ϵ centred at the point $(2, \frac{2}{3})$, where $\epsilon > 0$ is a small number, typically, $\epsilon = 0.1$. Therefore, on Γ_2, we impose the discontinuous flux

$$\frac{\partial u}{\partial n}(2, y) = g_1(y) = \begin{cases} \frac{1}{2\epsilon} & \text{if} \quad \frac{1}{3} - \epsilon \leq y \leq \frac{1}{3} + \epsilon, \\ \frac{-1}{2\epsilon} & \text{if} \quad \frac{2}{3} - \epsilon \leq y \leq \frac{2}{3} + \epsilon, \\ 0 & \text{otherwise.} \end{cases} \tag{8.1}$$

This experiment is typical of a two-electrode continuous model of electrical impedance/ resistance tomography (EIT/ERT), see e.g. [56, 57]. More realistic complete electrode models may also be considered [58].

We shall also investigate imposing the continuous flux

$$\frac{\partial u}{\partial n}(2, y) = g_2(y) = y(2 - y), \quad y \in (0, 2)\,, \tag{8.2}$$

being prescribed on Γ_2. Both fluxes (8.1) and (8.2) satisfy lateral continuity as we approach the corners $(2, 0)$ and $(2, 2)$ from either sides.

9 Numerical results for the direct problem (5.1)–(5.3)

For the corrosion coefficient we consider a positive space-dependent coefficient given by

$$\lambda(\theta) = \sin(\theta), \quad \theta \in \left(0, \frac{\pi}{2}\right), \tag{9.1}$$

on the boundary

$$\Gamma_0 = \left\{ (\cos(\theta), \sin(\theta)) |\ \theta \in \left(0, \frac{\pi}{2}\right) \right\}. \tag{9.2}$$

With λ given by (9.1) the linear and nonlinear Robin boundary conditions (3.1) and (4.1) recast as

$$\frac{\partial u}{\partial n} + \sin(\theta) u = 0, \quad \theta \in \left(0, \frac{\pi}{2}\right) \text{ on } \Gamma_0, \tag{9.3}$$

Table 1: Direct problem. The numerical BEM and MFS (with $\delta = 0.2$) solutions for the linear boundary condition (LBC) (9.3) and for the nonlinear boundary condition (NLBC) (9.4) on Γ_0, at arbitrary test points in Ω, for various $N \in \{10, 30, 90, 270\}$, when the discontinuous flux (8.1) is prescribed on Γ_2.

	N	u_{LBC}		u_{NLBC}	
		BEM	MFS	BEM	MFS
(1.5, 0.5)	10	0.0939	0.0526	0.0939	0.0526
	30	0.0732	0.0300	0.0732	0.0681
	90	0.0720	0.0712	0.0720	0.0712
	270	0.0717	0.0714	0.0717	
(1.5, 1.5)	10	-0.0724	-0.0690	-0.0724	-0.0689
	30	-0.0649	-0.0988	-0.0649	-0.0691
	90	-0.0659	-0.0665	-0.0659	-0.0666
	270	-0.0662	-0.0664	-0.0662	
(0.5, 1.5)	10	-0.0280	-0.0329	-0.0280	-0.0329
	30	-0.0274	-0.0539	-0.0274	-0.0308
	90	-0.0282	-0.0286	-0.0282	-0.0287
	270	-0.0284	-0.0285	-0.0284	

and

$$\frac{\partial u}{\partial n} + 2\sin(\theta)\sinh\left(\frac{u}{2}\right) = 0, \quad \theta \in \left(0, \frac{\pi}{2}\right) \text{ on } \Gamma_0, \tag{9.4}$$

respectively.

Since an analytical solution for the direct problem (5.1)–(5.3) is not available, we compare the numerical results obtained by using the BEM and MFS, previously introduced in sections 6 and 7, respectively. Numerical results are presented for the solution u along the boundaries Γ_0 and Γ_2 and inside the solution domain Ω.

Tables 1 and 2 show the convergence and the very good agreement obtained between the BEM and the MFS numerical solutions for u at various points in Ω, as $N = M/7$ or $\mathcal{M} = M$ increases. Further plots of the convergence of the BEM/MFS numerical solutions on the boundary $\partial\Omega$ can be found in [8] and therefore, they are not presented herein. We also note that the numerical MFS solution for the direct problem with the nonlinear boundary condition (9.4) for $\mathcal{M} = M = 7N = 7 \times 270$ could not be obtained due to extended computational processing times, preventing the completion of calculations in a reasonable time-frame. Therefore, only the BEM will be employed in the remaining of the paper.

Figures 2(a) and 2(c) shows that the BEM results for $u|_{\Gamma_0 \cup \Gamma_2}$ of the direct problem with the discontinuous flux (8.1) prescribed on Γ_2 and linear or nonlinear boundary conditions (9.3) or (9.4) on Γ_0 are very similar. This is to be expected since the linear and nonlinear functions (2.5) (with $u_a = 0$) and (2.6) are very close to each other for $|u|$ small, (see the small values of $u|_{\Gamma_0}$ in Figure 2(a)). On the other hand, when the continuous flux (8.2) is prescribed on Γ_2, the numerical BEM results for $u|_{\Gamma_0 \cup \Gamma_2}$ presented in Figures 2(b) and 2(d), obtained from solving the direct problem with linear or nonlinear boundary conditions (9.3) or (9.4) on Γ_0 are slightly different because $-2\sinh(\frac{u}{2})$ and $-u$ on Γ_0 start to become distinguishable for the larger values of $u|_{\Gamma_0}$ illustrated in Figure 2(b). The accurate values of $u|_{\Gamma_2}$ presented in Figures 2(c) and 2(d) will serve as input data for the inverse problems that will be investigated in the remaining of the paper.

Table 2: Direct problem. The numerical BEM and MFS (with $\delta = 0.2$) solutions for the linear boundary condition (LBC) (9.3) and for the nonlinear boundary condition (NLBC) (9.4) on Γ_0, at arbitrary test points in Ω, for various $N \in \{10, 30, 90, 270\}$, when the continuous flux (8.2) is prescribed on Γ_2.

	N	u_{LBC}		u_{NLBC}	
		BEM	MFS	BEM	MFS
(1.5, 0.5)	10	2.3208	2.0579	2.1965	1.9666
	30	2.1897	2.1069	2.0824	2.0101
	90	2.1516	2.1244	2.0492	2.0255
	270	2.1394	2.1304	2.0386	
(1.5, 1.5)	10	2.3168	2.0854	2.1986	1.9994
	30	2.2002	2.1277	2.0988	2.0365
	90	2.1668	2.1430	2.0701	2.0497
	270	2.1561	2.1482	2.0610	
(0.5, 1.5)	10	1.7158	1.5145	1.6044	1.4341
	30	1.6134	1.5507	1.5184	1.4654
	90	1.5844	1.5639	1.4939	1.4766
	270	1.5752	1.5684	1.4862	

Once the BEM solver has been tested for accuracy and convergence, the next sections 10–12 describe the iterative nonlinear minimization procedures developed for solving the inverse and ill-posed problems I-III, respectively.

10 Numerical solution of the inverse problem I given by equations (2.7) and (5.1)–(5.3) for the determination of the coefficient of corrosion

At the first glance, one could solve the linear but ill-posed Cauchy problem given by equations (5.1), (5.2) and (2.7), e.g., using the BEM with the truncated singular value decomposition for solving the resulting ill-conditioned system of equations, as described in [6, sections 4 and 5], after which attempt to retrieve the coefficient λ from (5.3) directly as

$$\lambda = \frac{\partial_n u}{f(u)} \quad \text{on } \Gamma_0, \tag{10.1}$$

as proposed in [47] for the linear Robin boundary condition (3.1). However, formula (10.1) is applicable only at points on Γ_0 at which $f(u)$ does not vanish, i.e., in the case of $f(u) = -2\sinh\left(\frac{u}{2}\right)$ or $f(u) = -u$ then these would be points at which u itself would not vanish. In addition, the reconstruction of the corrosion coefficient from (10.1) will be sensitive to errors in u in the vicinity of its zeros on Γ_0. Therefore, to obtain more stable solutions we solve simultaneously the equations (2.7) and (5.1)–(5.3). The inverse problem I given by equations (2.7), (5.1) and (5.2) in case of the linear boundary condition (3.1) has already been analysed in subsection 3.2. As for the numerical implementation, the discretisation of the boundary data (2.7) yields, using (6.2a),

$$u(\underline{p}) \equiv u(\tilde{p}_j) = u_j = h(\tilde{p}_j) = h_j \quad \text{for} \quad \underline{p} \in [\underline{p}_{j-1}, \underline{p}_j],\ j = \overline{2N+1, 4N}. \tag{10.2}$$

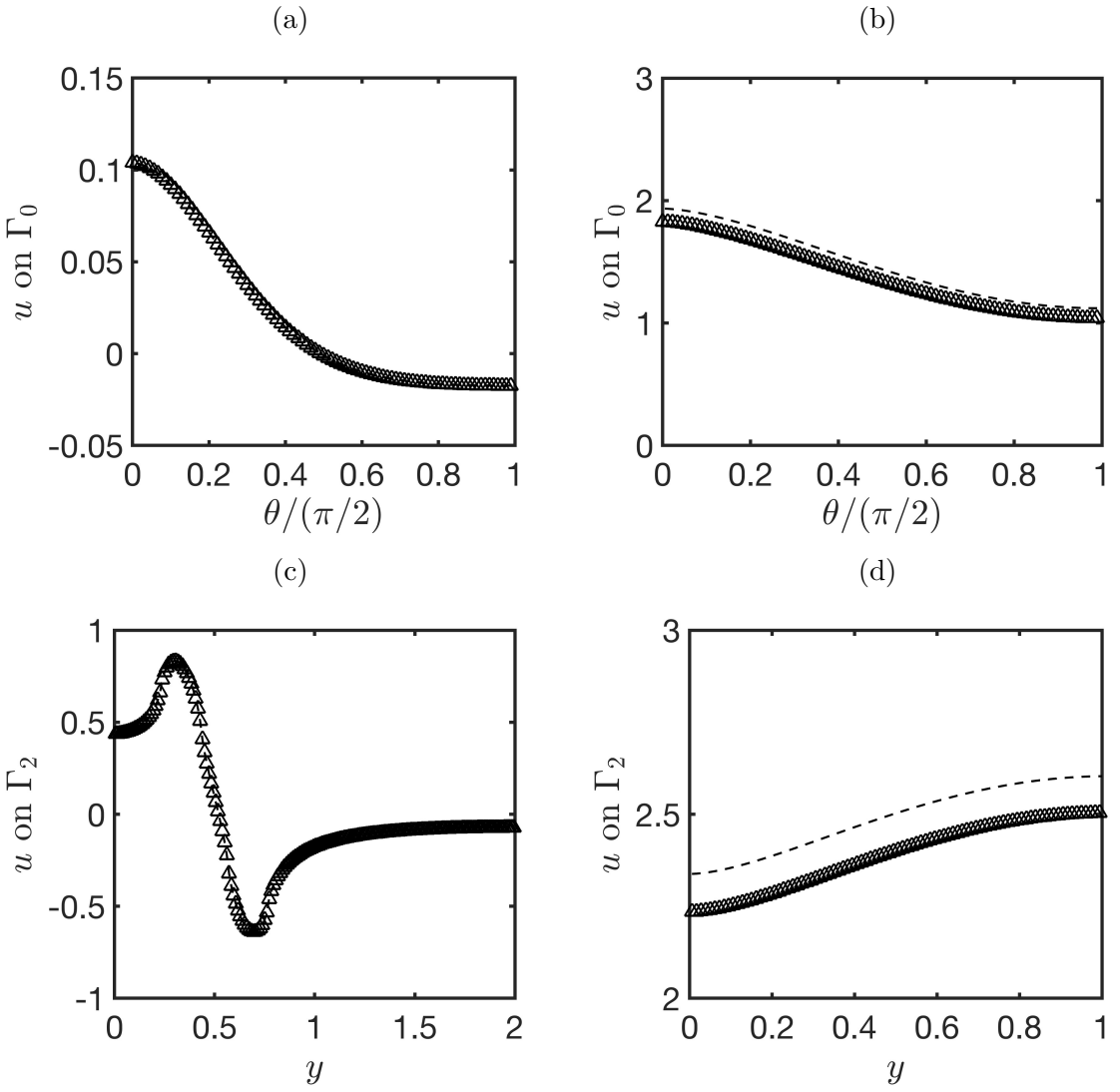

Figure 2: Direct problem. Comparison of the BEM numerical solutions for u on $\Gamma_0 \cup \Gamma_2$ obtained with $N = 90$ for the linear $(---)$ and nonlinear $(\triangle\triangle\triangle)$ boundary conditions (9.3) and (9.4), respectively, when (a,c) the discontinuous flux (8.1) and (b,d) the continuous flux (8.2) is prescribed on Γ_2.

Using the BEM introduced in section 6, the discretisation of the inverse problem I given by equations (2.7) and (5.1)–(5.3) gives the system of equations (6.2) (or (6.8)) and (10.2) in the unknowns $\underline{u} = (u_j)_{j=\overline{1,M}}$ and $\underline{\lambda} = (\lambda_j)_{j=\overline{1,N}}$. As such, this system of nonlinear equations is overdetermined having $M + 2N$ equations with $M + N$ unknowns.

As the objective is to minimize iteratively with respect to $\underline{\lambda}$ the discrepancy between the computed and the measured boundary potential (10.2), we eliminate $\underline{u} = (u_i)_{i=\overline{1,M}}$ from the system of equations (6.3), written as

$$D(\underline{\lambda}, \underline{u}) := \sum_{j=1}^{N} \left[A_{ij} \lambda_j f(u_j) + B_{ij} u_j \right] + \sum_{j=N+1}^{M} B_{ij} u_j = \underline{b}, \tag{10.3}$$

where $\underline{b} = (b_i)_{i=\overline{1,M}}$ with

$$b_i = - \sum_{j=2N+1}^{4N} A_{ij} g_j \quad \text{for} \quad i = \overline{1, M}.$$

In case of the linear law (2.5) with $u_a = 0$, the left-hand side of (10.3) can be written in matrix form as, see also (6.8),

$$D(\underline{\lambda}) \underline{u} = \underline{b}, \tag{10.4}$$

where

$$D_{ij}(\underline{\lambda}) = \begin{cases} B_{ij} - A_{ij} \lambda_j, & i = \overline{1, M},\ j = \overline{1, N}, \\ B_{ij}, & i = \overline{1, M},\ j = \overline{N+1, M}, \end{cases} \tag{10.5}$$

whose inversion eliminates $\underline{u}$ explicity, as given by

$$\underline{u}(\underline{\lambda}) = \left(D(\underline{\lambda}) \right)^{-1} \underline{b}. \tag{10.6}$$

In case of the nonlinear law (2.6) (and for other nonlinear laws) we can express $\underline{u}$ in terms of $\underline{\lambda}$ from (10.3) using the implicit function theorem, which is applicable since the direct problem (5.1)–(5.3) is uniquely solvable for any $\lambda \in \Lambda_{ad}$, as discussed in subsection 4.1. Based on this elimination (or on (10.6)) we can then construct the least–squares objective functional $F : \Lambda_{ad} \to \mathbb{R}_+$ given by

$$F(\lambda) = \| u(\lambda)|_{\Gamma_2} - h \|^2_{L^2(\Gamma_2)}, \tag{10.7}$$

or, in discretised form,

$$F(\underline{\lambda}) = \frac{2}{2N} \sum_{i=2N+1}^{4N} \left(u_i(\underline{\lambda}) - h_i \right)^2. \tag{10.8}$$

As seen from (10.7) or (10.8), the objective is to minimize the gap between the computed BEM solution for $u(\lambda)|_{\Gamma_2}$ and the measured boundary potential data h on Γ_2 given by (2.7). According to the analysis discussed in subsection 3.2, the set (3.4) guarantees that, as least for the linear law of corrosion (2.5), a solution $(u, \lambda) \in H^1(\Omega) \times \Lambda_{ad}$ to the inverse problem (2.7), (3.1), (5.1) and (5.2) with $0 \not\equiv g \in H^{-1/2}(\Gamma_2)$ is unique. However, since this solution will likely be unstable with respect to small noise in the measured data (2.7), a regularization term $R(\lambda)$ is often added to the least-squares functional (10.8) to yield the Tikhonov regularization functional

$$F_{reg}(\lambda) := F(\lambda) + \mu R(\lambda), \tag{10.9}$$

where $\mu \geq 0$ is a regularization parameter to be prescribed. If there exists *a priori* information on the regularity of the unknown function that is sought, e.g. of class C^k with $k \in \mathbb{N}$, then this can be imposed by choosing $R(\lambda)$ as the norm of the k-th order derivative of λ. Moreover, the choice of the regularization parameter μ can be based on the L-curve criterion [64] or on trial and error by selecting a small positive value of μ and then gradually increasing it until oscillations in the obtained solution disappear [54].

We mention that instead of the least-squares functional (10.7), the so-called Kohn-Vogelius functional minimizing the gap between the solution of the Neumann-Robin direct problem (5.1)–(5.3) and the Neumann-Dirichlet-Robin direct problem (2.7), (5.1), (5.3) and

$$\frac{\partial u}{\partial n} = 0 \quad \text{on } \Gamma_1 \cup \Gamma_3 \cup \Gamma_4, \tag{10.10}$$

may also be devised, see [35, 36, 74, 121] which considered the linear Robin boundary condition (3.1).

The discretised form of (10.9) subject to simple bounds on the variables $\underline{\lambda}$ is minimized using the Matlab toolbox routine `lsqnonlin`, starting from an arbitrary initial guess $\underline{\lambda}^{(0)}$ within those prescribed bounds and with the gradient computed internally by the routine using finite differences [70]. Integrated within the Matlab optimization toolbox, `lsqnonlin` supports various minimization algorithms such as the trust-reflective region (TRR) by default, Interior-point and Levenberg-Marquardt [51, 52, 70]. We have employed all these methods with similar performances and we have decided to use the TRR method which adjusts the solution based on residual reduction, balancing convergence and stability. Termination criteria such as Function Tolerance (gradient magnitude threshold) can be used to stop the iterations when changes become negligible.

10.1 Numerical results and discussion for inverse problem I

We consider the geometry depicted in Figure 1 with Γ_0 given by (9.2). We take the function g on Γ_2 given by equation (8.1), which corresponds to an injected discontinuous current flux in an EIT experiment and measure the resulting potential on Γ_2, as given by equation (2.7). We numerically simulate this data by solving the direct problem (5.1), (8.1) and (5.3) with λ given by (9.1), using a boundary mesh with $M = 7N = 630$ boundary elements, as described in section 6 and illustrated in Figure 2(c). This discretisation was found sufficiently fine to ensure that any further increase to, say $M = 7N = 1890$ boundary elements, did not significantly affect the accuracy of the numerical results. In the inverse problem, we utilize only a portion of this data, specifically one-third, on Γ_2, such that the BEM direct solver at each iteration of the minimization process is employed with $N = 30$ resulting in $M = 7N = 210$ boundary elements. This common numerical modelling approach of taking a different mesh for solving the direct and inverse problems when utilising the same discretisation method not only prevents committing an inverse crime [79], but it also introduces some numerical noise into the data (2.7).

Simple physical bounds on the variables $\underline{\lambda} = (\lambda_j)_{j=\overline{1,N}}$ are prescribed as

$$0 = \lambda_{min} \leq \lambda_j \leq \lambda_{max} = 1, \quad j = \overline{1, N}, \tag{10.11}$$

where corresponding to (6.2b) and (9.2), $\tilde{\underline{p}}_j = (\cos(\tilde{\theta}_j), \sin(\tilde{\theta}_j))$ and $\tilde{\theta}_j = \frac{\pi}{2}(1 - \frac{2j-1}{2N})$ for $j = \overline{1, N}$. The initial guess is taken as $\lambda_j^{(0)} = \frac{\tilde{\theta}_j}{\pi/2}$ for $j = \overline{1, N}$, which corresponds to the straight line $\lambda(\theta) = \frac{\theta}{\pi/2}$ for $\theta \in [0, \frac{\pi}{2}]$ joining the points specified according to (9.1) as

$\lambda(\pi/2) = 1$ and $\lambda(0) = 0$. The tolerance parameters employed in the `lsqnonlin` toolbox are set up at some small values, namely, Function Tolerance $= 10^{-20}$, Step Tolerance $= 10^{-20}$ and Optimality Tolerance $= 10^{-15}$. These tolerances are used throughout all computations performed in sections 10–12.

The choice of the regularization term $R(\lambda)$ in (10.9) depends on the *a priori* knowledge of the regularity of the sought corrosion coefficient λ to correspond to various degrees of derivative penalisation. Initially, we have tried using the zeroth-order regularization term $R(\lambda) = \|\lambda - \lambda^{(0)}\|^2_{L^2(\Gamma_0)}$, which penalises the function $\lambda \in C(\Gamma_0)$, such that the discretised form of (10.9) becomes (see also (10.8))

$$F_\mu(\underline{\lambda}) = \frac{2}{2N} \sum_{j=2N+1}^{4N} (u_j(\underline{\lambda}) - h_j)^2 + \mu \sum_{j=1}^{N} (\lambda_j - \lambda_j^{(0)})^2. \tag{10.12}$$

10.1.1 Results for the linear boundary condition (3.1)

Consider first the case of the linear boundary condition (3.1). Figure 3(a) provides valuable insight into the convergence of the zeroth-order regularization functional (10.12) with the number of iterations, for various regularization parameters $\mu \in \{0, 10^{-5}, 10^{-4}\}$. From this figure, it can be observed that the iterative process converges quickly to minimum small values, after which it remains stationary until it stops according to the imposed tolerances in the `lsqnonlin` routine.

Figure 3(b) provides a quantitative assessment of accuracy by plotting the error between the numerically recovered and exact coefficient of corrosion, against the regularization parameter μ. According to this figure, it can be seen that $\mu = 3 \times 10^{-6}$ is the optimal regularization parameter. Of course, this value is not available to us since λ_{exact} is not known, in general. However, we could experience by trial and error with various values of μ and observe the numerically retrieved solutions becoming stable enough to mitigate noise without over-smoothing and losing important details.

Figure 3(c) presents the numerically recovered coefficient λ with various regularization parameters $\mu \in \{0, 10^{-5}, 10^{-4}\}$ in comparison with the exact solution (9.1). The numerical results obtained with no regularization, i.e., with $\mu = 0$, jump between the upper and lower bounds in (10.11) as a manifestation of the instability of the nonlinear least-squares non-convex functional (10.7) (or (10.8)).

On the other hand, the numerical results obtained with the regularization parameter $\mu = 10^{-5}$ (or 10^{-4}) show a good balance between stability and accuracy; however, the obtained solution is still far from the exact solution (9.1). One possible way to improve the reconstruction is to increase the order of regularization, i.e. the solution smoothness, assuming that such physical information is available. Then, as illustrated in Figure 4, for $\mu = 10^{-5}$ better convergence and accuracy is obtained by penalising the first-order derivative of λ (assumed to be in $C^1(\Gamma_0)$) through the first-order Tikhonov regularization functional given by

$$F_\mu(\underline{\lambda}) = \frac{2}{2N} \sum_{j=2N+1}^{4N} (u_j(\underline{\lambda}) - h_j)^2 + \mu \sum_{j=2}^{N} (\lambda_j - \lambda_{j-1})^2. \tag{10.13}$$

Next, we perturb the exact data (2.7) by noise of percentage p, as given by,

$$h_j^{noisy} = h_j(1 + \mathrm{p}\rho_j), \quad j = \overline{2N+1, 4N}, \tag{10.14}$$

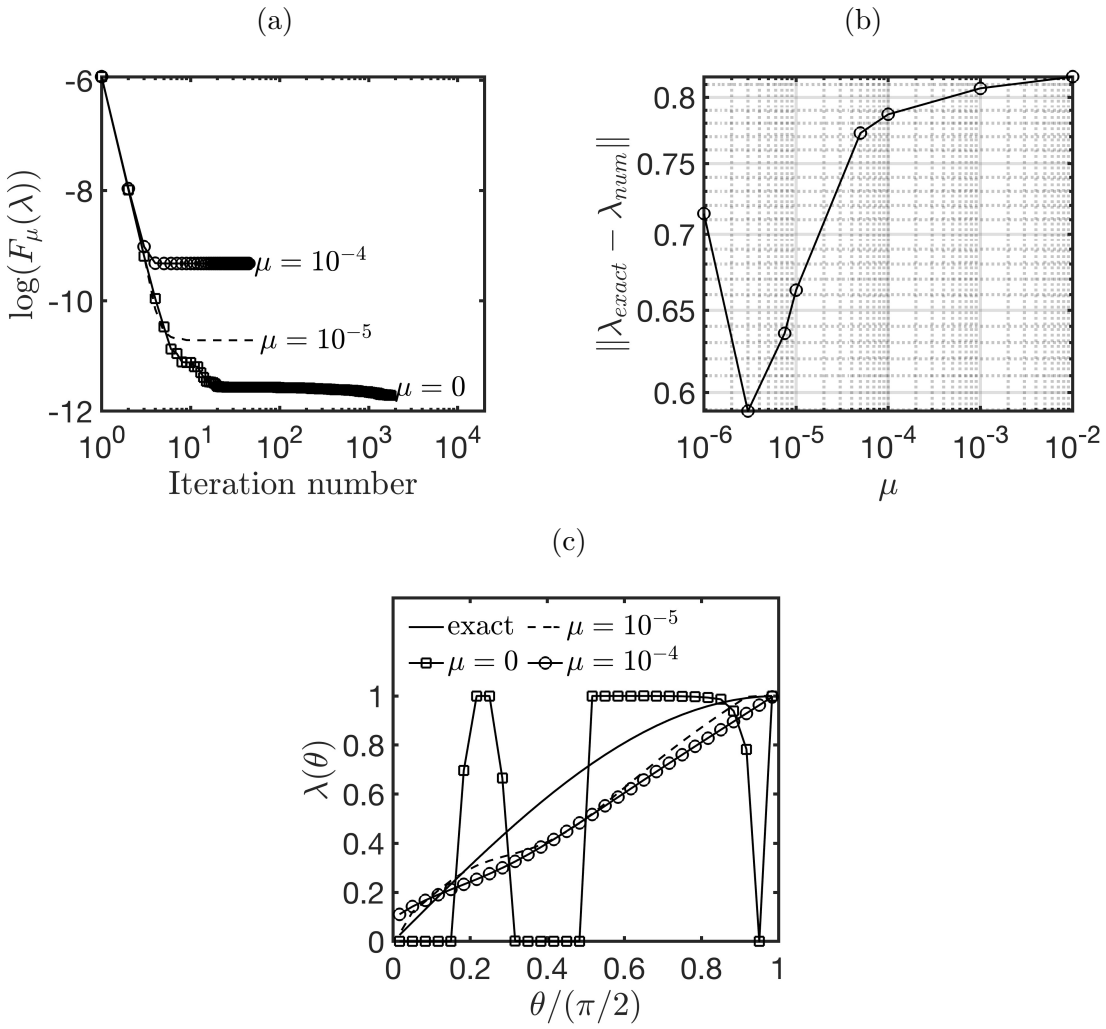

Figure 3: Inverse problem I with the linear boundary condition (9.3), no noise p = 0. Determining the corrosion coefficient $\lambda(\theta)$ on the boundary Γ_0 using the zeroth-order regularization with various values of the the regularization parameter μ. The figure shows: (a) the convergence of the objective function (10.12) with the number of iterations, (b) the norm of the difference between the exact and numerical solutions as a function of μ, and (c) the comparison between the exact and numerical solutions.

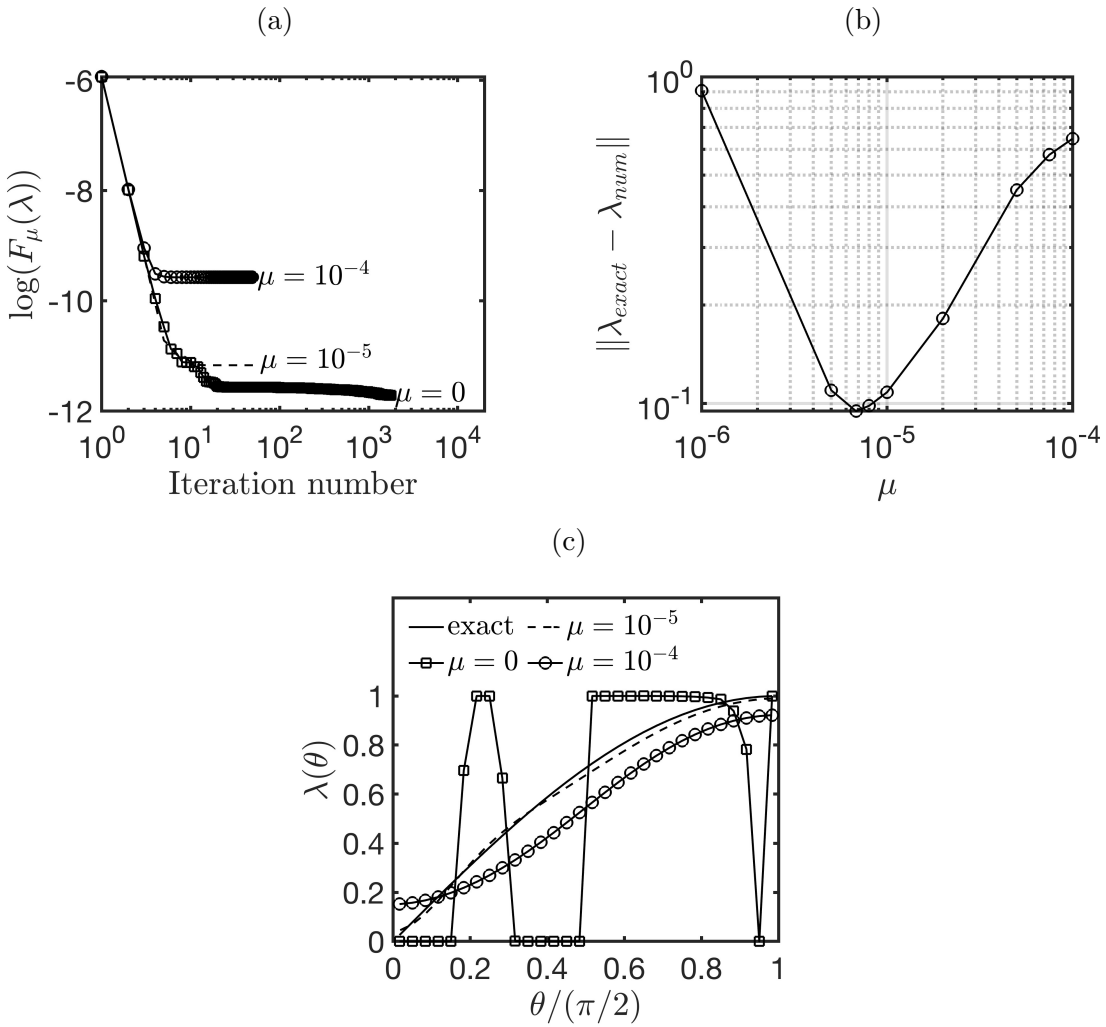

Figure 4: Inverse problem I with the linear boundary condition (9.3), no noise p = 0. Determining the corrosion coefficient $\lambda(\theta)$ on the boundary Γ_0 using the first-order regularization with various values of the the regularization parameter μ. The figure shows: (a) the convergence of the objective function (10.13) with the number of iterations, (b) the norm of the difference between the exact and numerical solutions as a function of μ, and (c) the comparison between the exact and numerical solutions.

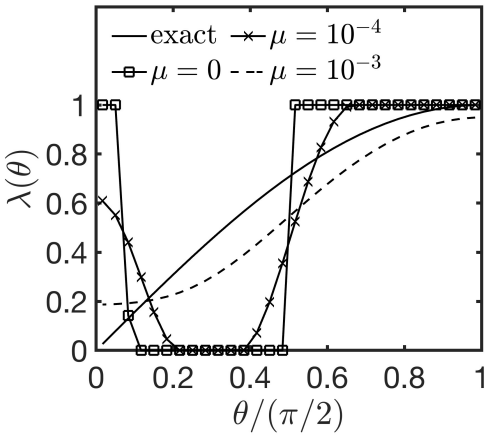

Figure 5: Inverse problem I with the linear boundary condition (9.3), noise p = 1%. Determining the corrosion coefficient $\lambda(\theta)$ on the boundary Γ_0 using the first-order regularization (10.15) with various values of the regularization parameter μ.

where ρ_j are random variables drawn from a uniform distribution in $[-1, 1]$, in order to test the stability of the regularization process under small errors in the input measured data. Noise makes the recovery of the unknowns more sensitive, but by choosing an appropriate regularization parameter μ, we can still obtain reliable, i.e. stable and accurate, results. Confidence, or credibility, intervals of the recovered solutions may be established by repeating the inversion process for a few random noise simulations in (10.14) and then averaging the obtained results [53].

Based on the previous results obtained in Figures 3 and 4 in case p = 0, we further employ only the first-order regularization functional (10.13) with h_j being replaced by h_j^{noisy} for $j = \overline{2N+1, 4N}$, given by

$$F_\mu(\underline{\lambda}) = \frac{2}{2N} \sum_{j=2N+1}^{4N} (u_j(\underline{\lambda}) - h_j^{noisy})^2 + \mu \sum_{j=2}^{N} (\lambda_j - \lambda_{j-1})^2. \tag{10.15}$$

We note that in practice the noisy data comes from measurement, which inherently contains errors, and in our numerical simulations we do not make any assumption about the type of noise with which this data is contaminated.

Figure 5 shows the numerical recoveries of λ in case of inverting p = 1% noisy data. On comparing with Figure 4(c) where p = 0 no noisy data were inverted, from Figure 5 it can be seen that noise causes some inaccuracies between the exact and numerical solutions, but the overall stable pattern and reasonable accuracy is still captured for $\mu = 10^{-3}$. This shows that the first-order Tikhonov regularization method is fairly stable with respect to noise in the input data, provided that the regularization parameter μ is chosen appropriately to control the balance between noise reduction and solution's accuracy.

10.1.2 Results for the nonlinear boundary condition (4.1)

In case of the Butler-Volmer law of corrosion (2.6), the nonlinear Robin boundary condition is given by (4.1). In case of no noise, i.e. p = 0, the results presented in Figure 6 show similar features to those presented in Figure 4 obtained for the linear boundary

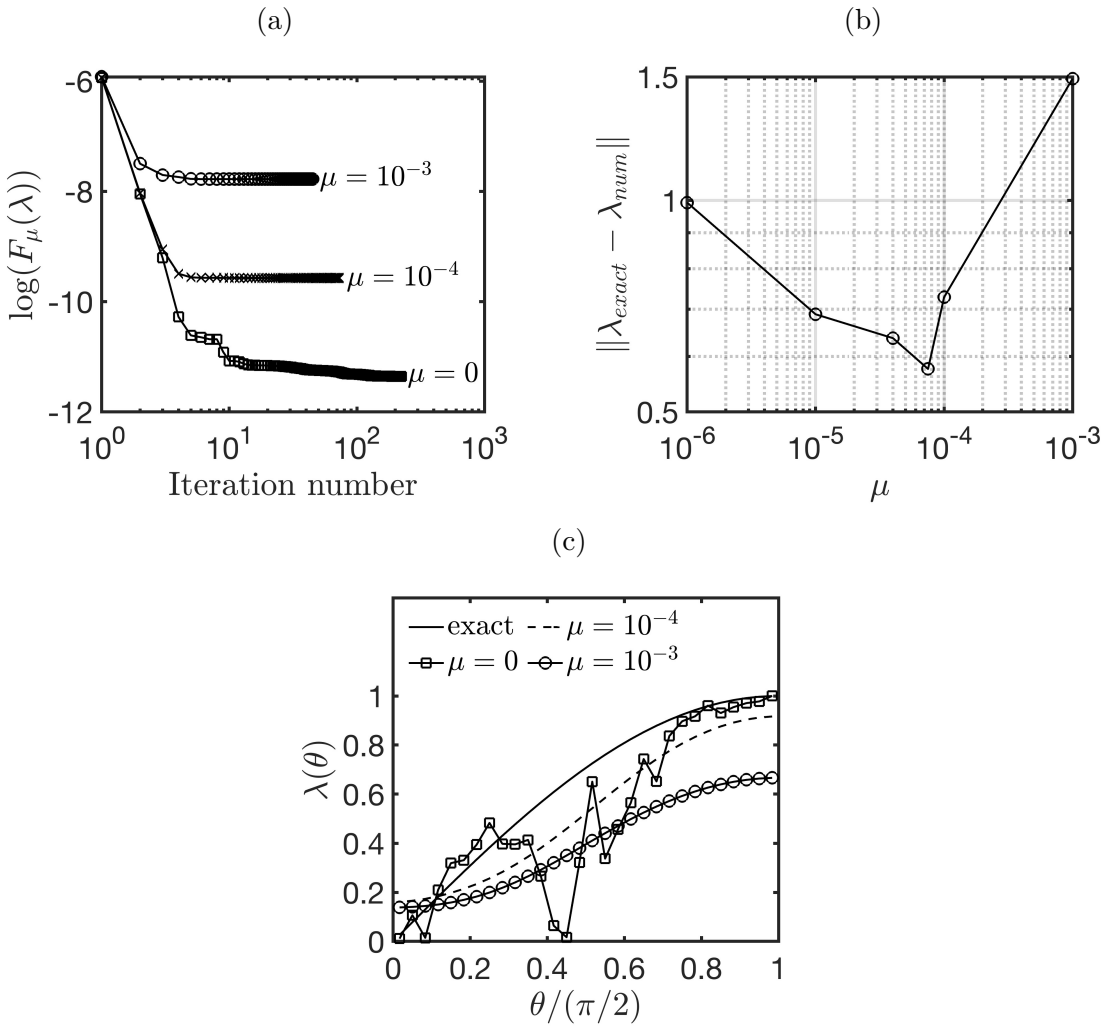

Figure 6: Inverse problem I with the nonlinear boundary condition (9.4), no noise p = 0. Determining the corrosion coefficient $\lambda(\theta)$ on the boundary Γ_0 using the first-order regularization with various values of the the regularization parameter μ. The figure shows: (a) the convergence of the objective function (10.13) with the number of iterations, (b) the norm of the difference between the exact and numerical solutions as a function of μ, and (c) the comparison between the exact and numerical solutions.

condition (3.1). However, the less accurate results obtained in Figure 6(c) compared to those of Figure 4(c) indicate that the nonlinear boundary condition (4.1) introduces extra computational challenges causing the functional (10.13) that is minimized becoming trapped perhaps in a local minimum. Improved results may be obtained by reducing the number N of unknown λ_i for $i = \overline{1, N}$, using a smaller finite set of trigonometric polynomials [21] for approximating $\lambda(\theta)$, as it will be illustrated later on for the inverse problem III in section 12.

11 Numerical solution of the inverse problem II given by equations (2.9), (5.1), (5.3), (8.1), (8.2) and (10.10)

The inverse problem II in the case of the linear boundary condition (3.1) has already been discussed in subsection 3.3. This section investigates the numerical reconstruction of the corroded boundary Γ_0 when using two pairs of Cauchy data formed from the fluxes (8.1) and (8.2) and the corresponding potentials (2.9) for $i = 1$ and 2.

Previously, the determination of a perfectly conductive (in case $\lambda = \infty$) or insulated (in case $\lambda = 0$) corroded part Γ_0 of the boundary $\partial\Omega$, formulated as a Cauchy linear problem in electrostatics governed by the Laplace's equation (2.1), was investigated using the BEM or the MFS combined with the level-set method in [96, 119, 120]. The BEM or the MFS was also combined with the Tikhonov regularization method to solve the same inverse problem in [93, 98]. For some special rectangular geometries, analytical treatment based on Fourier series is also possible [95]. The measurements (2.9) of the potential on Γ_2 are numerically simulated, as described in section 10, by solving the direct problem (5.1)–(5.3) with λ given by (9.1) and Γ_0 given by (9.2). This data was previously presented in Figures 2(c) and 2(d), as obtained using the BEM with $N = 90$. As in section 10, in order to prevent committing an inverse crime in the inverse problem we retain only a third of this data and apply the iterative BEM direct solver using $N = 30$.

We seek the unknown corroded boundary Γ_0 as part of a star-shaped domain with respect to the origin, parametrised as [7, 82]

$$\Gamma_0 = \Big\{ r(\theta)\,(\cos(\theta), \sin(\theta)) \,|\, \theta \in [0, \pi/2] \Big\}. \tag{11.1}$$

Alternatively, Γ_0 could be sought as the graph of an unknown function defined by $\Gamma_0 = \big\{(x, y(x)) | x \in (0, 1)\big\}$, as in [40, 93, 95]. In the absence of such physics-informed assumptions on the unknown corroded boundary, the level set method [83, 107] may be an option, but for its difficulty in accommodating the Robin boundary condition (2.3) and the high sensitivity to noise in the measured data.

In the particular cases that the linear Robin boundary condition (3.1) degenerates into a homogenous Neumann (for $\lambda = 0$) or Dirichlet (for $\lambda = \infty$) boundary condition, as reviewed in section 3.3, the corroded boundary Γ_0 can be uniquely identified from the single potential measurement (2.7) corresponding to the flux (2.2) and numerical reconstructions were attempted using a boundary collocation method in [119], the method of lines in [96], the MFS in [98, 120] and the BEM in [93].

In accordance with the BEM discretization described in section 6, the endpoints of the boundary elements discretising Γ_0 given by (11.1) have the coordinates $\underline{p}_j = (r(\theta_j)\cos(\theta_j), r(\theta_j)\sin(\theta_j))$ for $j = \overline{0, N}$, with $\theta_j = \frac{\pi(N-j)}{2N}$, where $r(\theta_0) = r\left(\frac{\pi}{2}\right) = 1$ and $r(\theta_N) = r(0) = 1$. Denoting by $r_j := r(\theta_j)$ for $j = \overline{1, N-1}$, the inverse problem then seeks the vector $\underline{r} = (r_j)_{j=\overline{1,N-1}}$ which minimizes the functional

$$C(\underline{r}) := \sum_{i=1}^{2} \|u^{(i)}(\underline{r}) - h^{(i)}\|^2_{L^2(\Gamma_2)}, \tag{11.2}$$

where $u^{(i)}(\underline{r}; \cdot)|_{\Gamma_2}$ is the computed solution from the BEM system of equations (6.3) for

a given $\underline{r}$. In discretised form (11.2) becomes

$$C(\underline{r}) = \frac{2}{2N} \sum_{i=1}^{2} \sum_{j=2N+1}^{4N} \left(u_j^{(i)}(\underline{r}) - h_j^{(i)} \right)^2 . \tag{11.3}$$

Simple bounds on the variables such as

$$r_{min} \leq r_j \leq r_{max} \quad \text{for } j = \overline{1, N-1} \tag{11.4}$$

are imposed, and the constrained minimization problem is solved iteratively using the `lsqnonlin` based on the TRR algorithm, as in section 10, starting from an arbitrary initial guess $\underline{r}^{(0)} = \left(r_j^{(0)} \right)_{j=\overline{1,N-1}}$ satisfying the constraints (11.4).

Especially, in case the measured potential data on Γ_2 is contaminated with noise, as in (10.14), namely,

$$h_j^{(i)noisy} = h_j^{(i)}(1 + \mathrm{p}\rho_j), \quad j = \overline{2N+1, 4N},\ i = 1, 2, \tag{11.5}$$

the functional (11.3) has to be penalized resulting in the regularized functional (of zeroth-order) given by

$$C_\mu(\underline{r}) = \frac{2}{2N} \sum_{i=1}^{2} \sum_{j=2N+1}^{4N} \left(u_j^{(i)}(\underline{r}) - h_j^{(i)noisy} \right)^2 + \mu \sum_{j=1}^{N-1} \left(r_j - r_j^{(0)} \right)^2 . \tag{11.6}$$

11.1 Numerical results and discussion for inverse problem II

We consider two examples of corroded boundary Γ_0 given by a quarter of the unit circle (Example 1), i.e.,

$$r(\theta) = 1, \quad \theta \in \left[0, \frac{\pi}{2}\right], \tag{11.7}$$

and a straight-line segment joining the points (0,1) and (1,0), (Example 2), i.e.,

$$r(\theta) = \frac{1}{\sqrt{2}\sin(\theta + \pi/4)}, \quad \theta \in \left[0, \frac{\pi}{2}\right]. \tag{11.8}$$

The lower and upper bounds in (11.4) are taken as

$$r_{min} = \begin{cases} 0.5 & \text{for Example 1,} \\ 0.7 & \text{for Example 2,} \end{cases} \qquad \text{and} \qquad r_{max} = \begin{cases} 1.5 & \text{for Example 1,} \\ 1.1 & \text{for Example 2.} \end{cases} \tag{11.9}$$

We take $\lambda \equiv 1$ which also ensures that the direct problem given by (5.1), (5.2) and the linear or nonlinear boundary conditions (3.1) or (4.1) given by

$$\frac{\partial u}{\partial n} + u = 0 \quad \text{on } \Gamma_0, \tag{11.10}$$

or

$$\frac{\partial u}{\partial n} + 2\sinh\left(\frac{u}{2}\right) = 0 \quad \text{on } \Gamma_0, \tag{11.11}$$

is well-posed, as discussed in sections 3.1 and 4.1.

We investigate the reconstruction of the polar radius $r(\theta)$, discretised in the form of the vector $\underline{r} = (r_j)_{j=\overline{1,N-1}}$, which yields Γ_0 through the star-shape representation (11.1), from the two pairs of data (2.8) and (2.9) induced by the current flux (8.1) and (8.2).

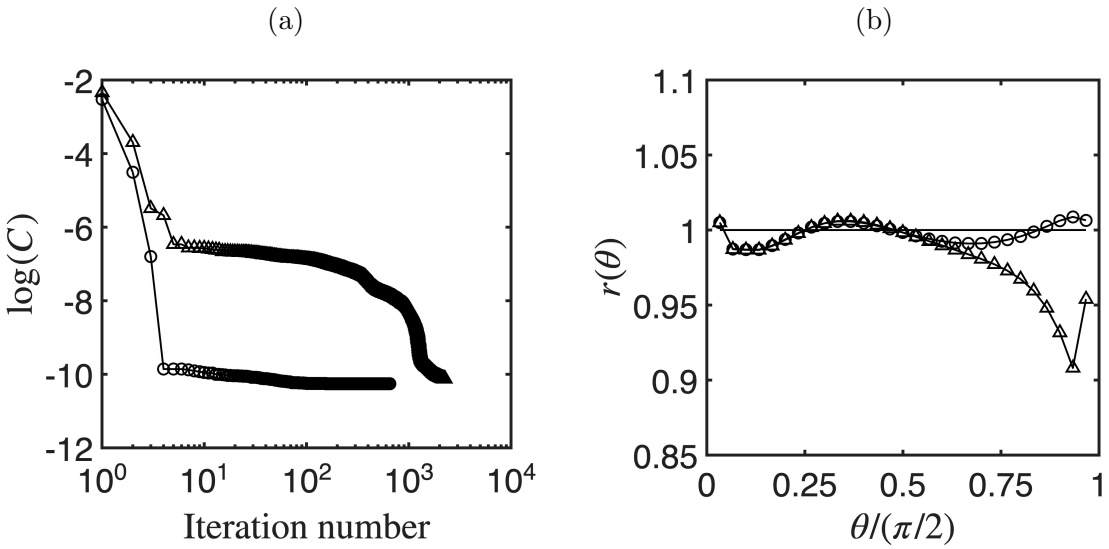

Figure 7: Inverse problem II. No noise, no regularization (Example 1 with the linear boundary condition (11.10)). The figure shows: (a) the convergence of the objective function (11.3) with the initial guess (11.12) shown with $(- \circ -)$ and with the initial guess (11.13) shown with $(-\Delta-)$, along with the corresponding (b) the numerical reconstructions of $r(\theta)$ in comparison with the exact solution (11.7) shown with (——).

Example 1

We first mention that inverting individually each of the boundary data (2.8) and (8.1) or (2.9) and (8.2) led to different results, see [7], for the two initial guesses

$$r^{(0)}(\theta) = 1.1, \quad \theta \in \left[0, \frac{\pi}{2}\right], \tag{11.12}$$

and

$$r^{(0)}(\theta) = \frac{1}{\sqrt{2}\sin(\theta + \pi/4)}, \quad \theta \in \left[0, \frac{\pi}{2}\right]. \tag{11.13}$$

This is expected since the inverse problem II with a single Cauchy data may not have a unique solution for Γ_0 in case of the Robin boundary condition (3.1) or (4.1), as pointed out in section 3.3. By using the two sets of Cauchy data (2.8) and (2.9) induced by the current fluxes (8.1) and (8.2), the functional (11.3) is minimized subject to the simple bounds on variables (11.4) with $r_{min} = 0.5$ and $r_{max} = 1.5$ and the initial guesses (11.12) or (11.13). The resulting numerical results for Example 1 with the linear boundary condition (11.10) are presented in Figure 7. As illustrated in Figure 7(a), the initial guess (11.13), which is farther away from the exact solution (11.7) than the initial guess (11.12), requires a larger number of iterations to achieve a small convergence threshold of 10^{-10} for the objective function (11.3). The numerical results for $r(\theta)$ illustrated in Figure 7(b) show some level of dependency on the initial guess; however, the reconstructions are reasonable in terms of accuracy.

Next, on considering the noisy data (11.5) for p = 1% we minimize the regularized objective functional (11.6) subject to the bounds (11.4) with $r_{min} = 0.5$ and $r_{max} = 1.5$, and illustrate in Figure 8 the results obtained with the initial guess (11.12) only for Example 1 with the linear boundary condition (11.10).

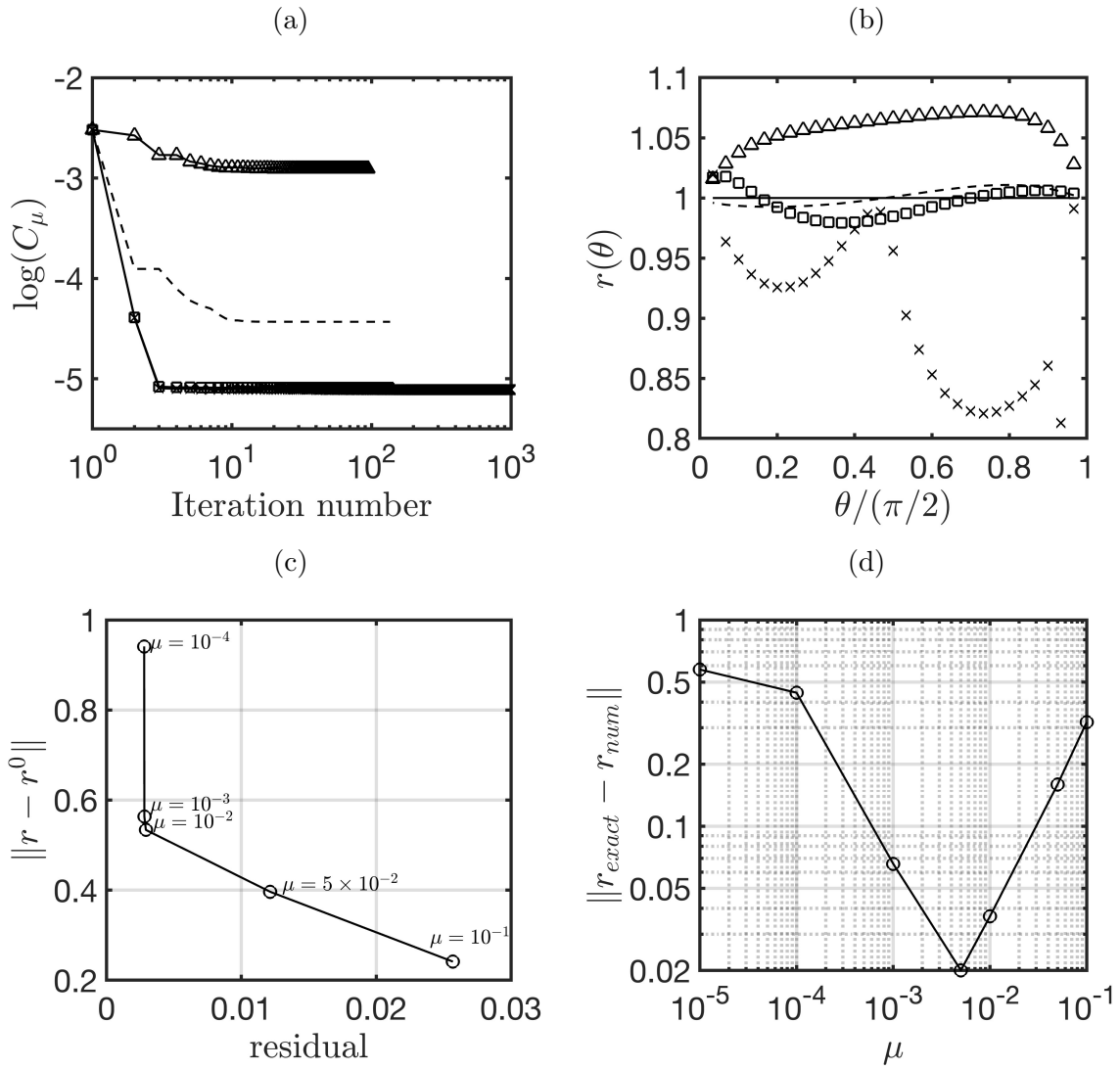

Figure 8: Inverse problem II. Noise p = 1%, with regularization (Example 1 with the linear boundary condition (11.10)). The figure shows: (a) the convergence of the objective function (11.6) with the initial guess (11.12), shown for different values of the regularization parameter: $(- \times -)$ for $\mu = 0$, $(-\square-)$ for $\mu = 10^{-3}$, $(- - -)$ for $\mu = 10^{-2}$ and $(-\Delta-)$ for $\mu = 10^{-1}$, along with the corresponding (b) the numerical reconstructions of $r(\theta)$ in comparison with the exact solution (11.7) shown with (——), (c) the L-curve, plotting the residual (11.3) versus the norm of $(r - r^0)$, and (d) the norm of the error, as a function of the regularization parameter.

Figure 8(a) shows the logarithm of the objective function (11.6) plotted against the iteration number. From this figure, it can be seen that in the absence of regularization, i.e. $\mu = 0$, the objective function (11.3) converges slowly, requiring about 1200 iterations to stabilise around 10^{-5}. In contrast, the minimization of (11.6) with $\mu = 10^{-2}$ reaches a stationary threshold of about 10^{-4} after only 100 iterations. The numerical results for the reconstructed polar radius $r(\theta)$ are illustrated in Figure 8(b) for various regularization parameters $\mu \in \{0, 10^{-3}, 10^{-2}, 10^{-1}\}$. For $\mu = 0$, the solution exhibits noticeable unphysical oscillations and deviates significantly from the exact solution (11.7), as expected since the inverse problem II is unstable with respect to small errors in the measured data (11.5). However, by regularising with $\mu = 10^{-2}$ shows considerable improved agreement between the numerical and exact solutions. This demonstrates the role of regularization in mitigating instabilities caused by the noise in the data. In Figure 8(c) we illustrate that the regularization parameter can be chosen at the corner of the L–curve resulting from plotting the residual (11.3) versus the norm of $\left(\underline{r} - \underline{r}^{(0)}\right)$. The obtained corner value corresponding to $\mu = 10^{-2}$ offers the best compromise between data fidelity and solution's smoothness, suggesting it as a suitable regularization parameter under the given noisy conditions, see [64] for more details on the L–curve. For completeness, Figure 8(d) shows the error norm between the exact and numerical solutions, as a function of the regularization parameter. The highest error occurs at $\mu = 0$ and the lowest at $\mu = 10^{-2}$, corroborating the earlier observations from the L–curve presented in Figure 8(c). This further validates the ability of the Tikhonov regularization in improving the accuracy and stability of the corroded shape reconstruction from the noisy data (11.5).

Next, on considering Example 1 with the nonlinear boundary condition (11.11), Figure 9 illustrates the numerically obtained results from the minimization of (11.6), the simple bounds on variables (11.4) with $r_{min} = 0.5$ and $r_{max} = 1.5$ and the initial guess (11.12). From this figure it can be seen an excellent recovery of the exact solution (11.7) from both exact and noisy data, illustrating also that the nonlinearity of (11.11) absorbs some of the instability with respect to the noise in (11.5) and, as a consequence, the use of regularization is not so crucial, as previously needed for the linear boundary condition (11.10) in Figure 8(b).

Example 2

Consider now Example 2, which seeks retrieving the shape (11.8) from the minimization of (11.6), the simple bounds on variables (11.4) with, see (11.9), $r_{min} = 0.7$ and $r_{max} = 1.1$, and the initial guess $r^{(0)} = 1$. Results are presented for various regularization parameters μ and for exact p = 0 and p = 1% noisy data. In particular, for the linear boundary condition (11.10) and noiseless p = 0 data, numerical results are presented in Figure 10. Figure 10(a) shows the convergence behaviour of the objective functional (11.6), as a function of the number of iterations, for various regularization parameters $\mu \in \{0, 10^{-3}, 10^{-2}, 10^{-1}\}$. The numerical results presented in Figure 10(b) show that regularization improves the solution's quality. The unregularized solution obtained with $\mu = 0$ exhibits some inaccuracies, which are removed by regularization with $\mu = 10^{-4}$ or 10^{-3}.

Figure 11 shows the corresponding results of Figure 10 when p = 1% noise is introduced in the data (11.5). Figure 11(a) shows that without regularization, the convergence of the objective function (11.3) is achieved in a large number of 10,000 iterations; how-

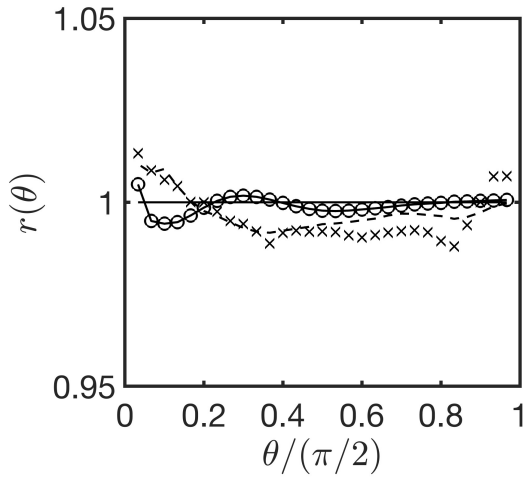

Figure 9: Inverse problem II. Numerical reconstructions of $r(\theta)$ in comparison with the exact solution (11.7) shown with (——) for Example 1 with the nonlinear boundary condition (11.11) and the initial guess (11.12). The line styles are: $(-\circ-)$ for p = 0 and $\mu = 0$, $(-\times-)$ for p = 1% and $\mu = 0$, and $(---)$ for p = 1% and $\mu = 10^{-3}$.

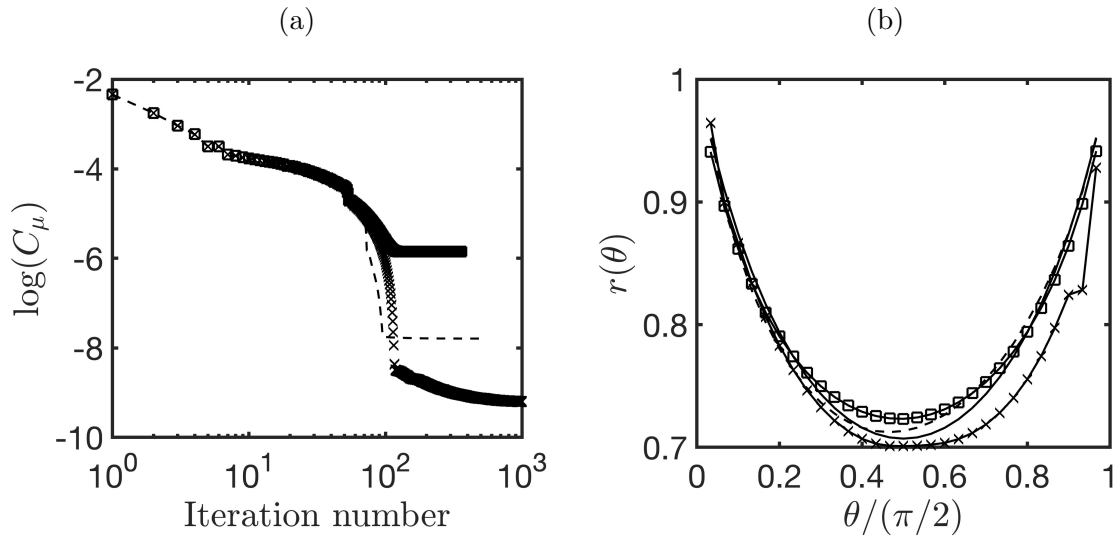

Figure 10: Inverse problem II. No noise, with regularization (Example 2 with the linear boundary condition (11.10)). The figure shows: (a) the convergence of the objective function (11.3), shown for different values of the regularization parameter: $(-\times-)$ for $\mu = 0$, $(---)$ for $\mu = 10^{-4}$ and $(-\square-)$ for $\mu = 10^{-3}$, along with the corresponding (b) numerical reconstructions of $r(\theta)$ in comparison with the exact solution (11.8) shown with (——).

ever, when regularization with $\mu = 5 \times 10^{-3}$ is applied, the convergence of the objective function (11.6) is achieved in only 500 iterations, demonstrating enhanced computational efficiency. The corresponding numerical results for $r(\theta)$ obtained with $\mu = 0$ and 5×10^{-3} are presented in Figure 11(b). From this figure it can be seen that the inaccuracies in the unregularized numerical solution are suppressed by the regularization with $\mu = 5 \times 10^{-3}$, which yields stable and accurate reconstruction of the exact solution (11.13).

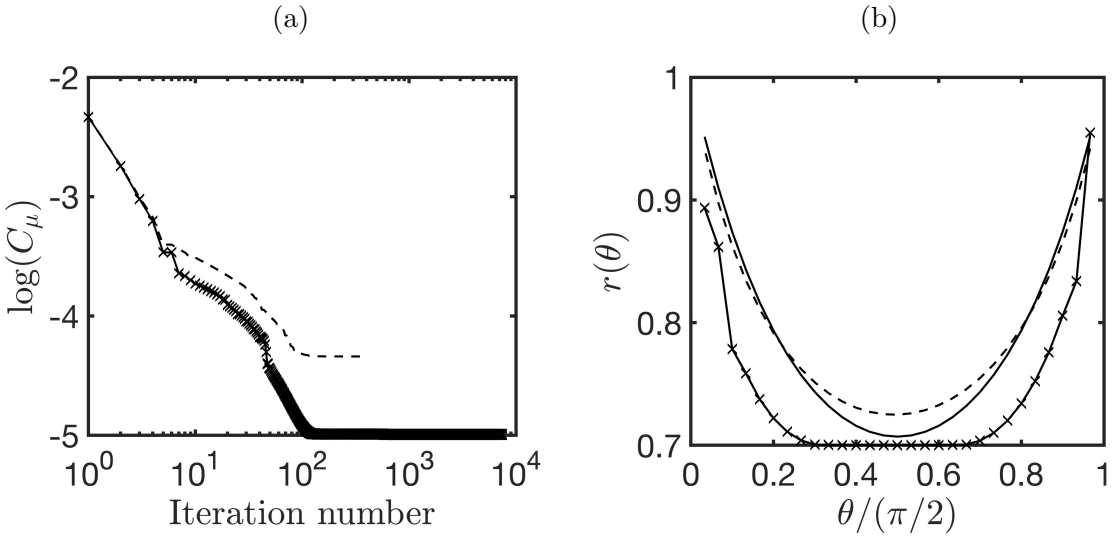

Figure 11: Inverse problem II. Noise p = 1% (Example 2 with the linear boundary condition (11.10)). The figure shows: (a) the convergence of the objective function (11.6), shown for different values of the regularization parameter: $(-\times-)$ for $\mu = 0$ and $(---)$ for $\mu = 5 \times 10^{-3}$, along with the corresponding (b) numerical reconstructions of $r(\theta)$ in comparison with the exact solution (11.8) shown with (——).

Next on considering Example 2 with the nonlinear boundary condition (11.11), Figure 12 illustrates the numerically obtained results from the minimization of (11.6), with the simple bounds on the variables (11.4) with $r_{min} = 0.7$ and $r_{max} = 1.1$, and the initial guess $r^{(0)} = 1$ for p $\in \{0, 1\%\}$ noisy data (11.5). As previously observed from Figure 9 for Example 1, the nonlinearity of (11.11) absorbs the instability with respect to the noise in (11.5) and therefore, the use of regularization was not found necessary.

12 Numerical solution of the inverse problem III

In this section, we combine the previous inverse problems I and II into requiring the simultaneous identification of the triplet solution (λ, Γ_0, u) with $\lambda \in \Lambda_{ad}, u \in H^1(\Omega)$ and Γ_0 star-shaped parametrised by (11.1), satisfying equations (5.1), (5.3), (10.10) and two pairs of Cauchy data (2.8) and (2.9). We consider the exact values for $\lambda(\theta)$ and $r(\theta)$ given by the sine function (9.1) and the circular boundary (11.7).

As discussed in section 3.4 in case of the linear corrosion (2.5), the uniqueness of solution of the problem (5.1), (3.1), (10.10), (8.1), (8.2) and (2.9) is ensured since the fluxes (8.1) and (8.2) are functionally independent and $g_2 > 0$, see [16]. Alternatively, we can employ the argument that h_1 and h_2 in Figures 2(c) and 2(d) are functionally independent and $h_2 > 0$, see [103]. Nevertheless, the joint inverse problem III addressed in this section is inherently more unstable than the individual inverse sub-problems I and

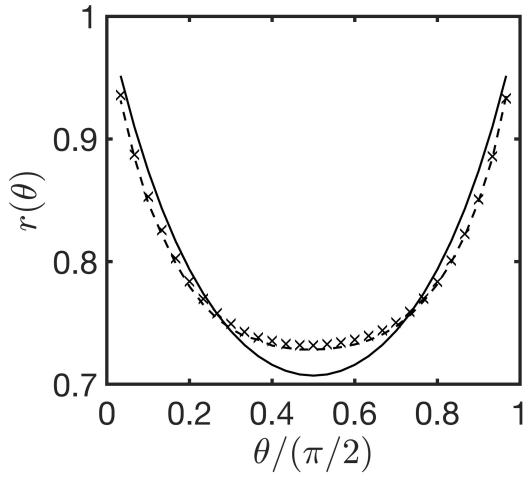

Figure 12: Inverse problem II. Numerical reconstructions of $r(\theta)$ in comparison with the exact solution (11.8) shown with (——) for Example 2 with the nonlinear boundary condition (11.11). The line styles are: $(- \times -)$ for p = 0 and $\mu = 0$, and $(- - -)$ for p = 1% and $\mu = 0$.

II examined in the sections 10 and 11, respectively. It combines the instability associated to recovering unknown geometries with the sensitivity inherent in reconstructing spatially varying Robin parameters, while introducing additional nonlinearity due to the coupling between the two unknowns [59].

By combining the previous objective functions (10.13) and (11.6) we minimize

$$S_{\mu_\lambda,\mu_r}(\underline{\lambda},\underline{r}) = \frac{2}{2N}\sum_{i=1}^{2}\sum_{j=2N+1}^{4N}\left(u_j^{(i)}(\underline{\lambda},\underline{r}) - h_j^{(i)}\right)^2 + \mu_\lambda\sum_{j=2}^{N}(\lambda_j-\lambda_{j-1})^2 + \mu_r\sum_{j=1}^{N-1}\left(r_j - r_j^{(0)}\right)^2, \quad (12.1)$$

where $\mu_\lambda \geq 0$ and $\mu_r \geq 0$ are regularization parameters to be prescribed, or its unregularized least-squares version

$$S(\underline{\lambda},\underline{r}) = \frac{2}{2N}\sum_{i=1}^{2}\sum_{j=2N+1}^{4N}\left(u_j^{(i)}(\underline{\lambda},\underline{r}) - h_j^{(i)}\right)^2. \quad (12.2)$$

As in (10.11) and (11.9), we consider the lower and upper bounds

$$0 = \lambda_{min} \leq \lambda_j \leq \lambda_{max} = 1,\ j = \overline{1,N}, \quad 0.5 = r_{min} \leq r_j \leq r_{max} = 1.5,\ j = \overline{1,N-1}, \quad (12.3)$$

and the initial guess

$$\lambda_j^{(0)} = \frac{\tilde{\theta}_j}{\pi/2},\ j = \overline{1,N}, \quad r_j^{(0)} = 1.1,\ j = \overline{1,N-1}. \quad (12.4)$$

The above constrained minimization problem is solved using the MATLAB toolbox routine `lsqnonlin`, as previously employed for solving the inverse problems I and II in

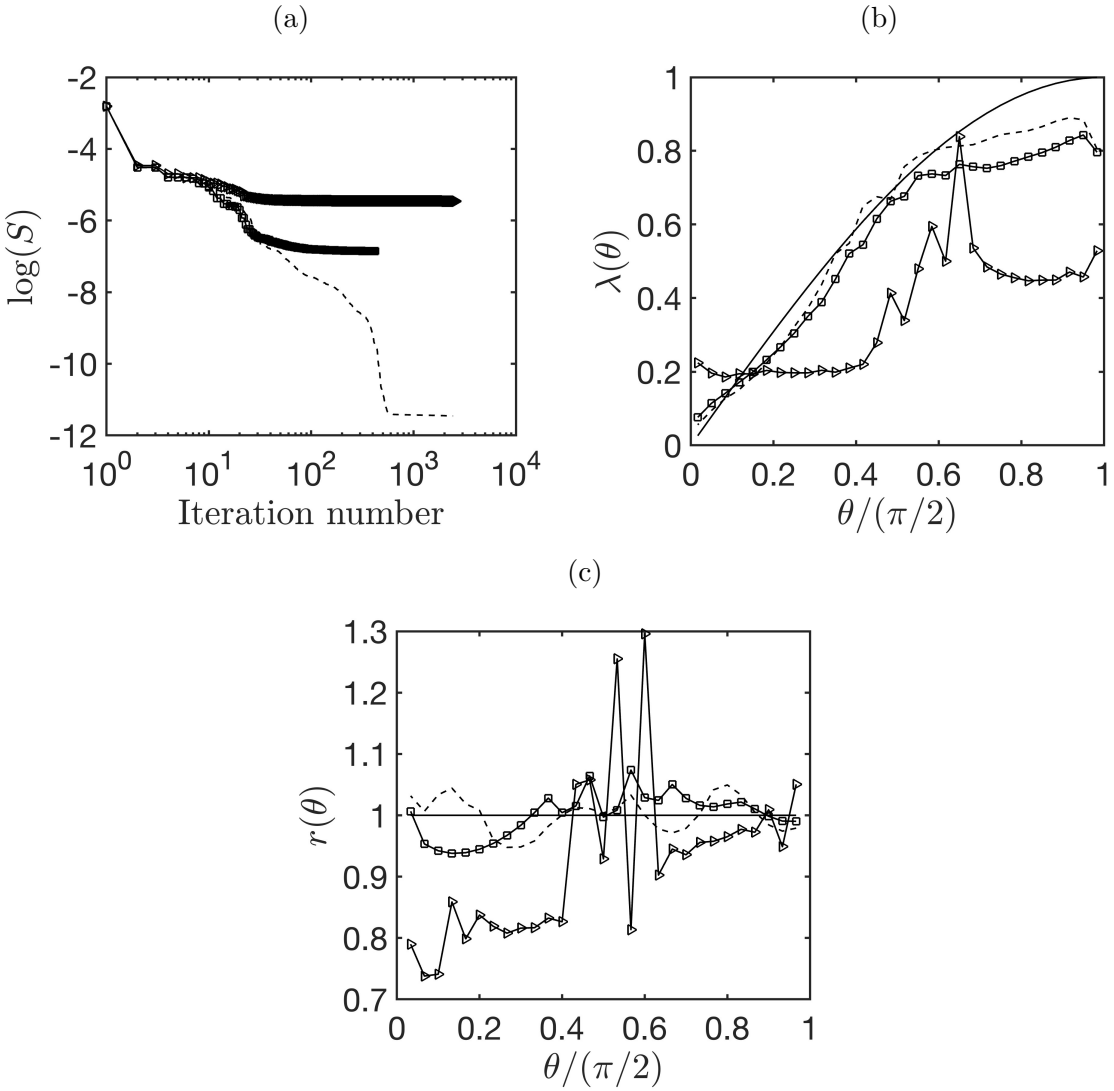

Figure 13: Inverse problem III. Numerical results obtained without regularization for the linear boundary condition (3.1) for different noise levels: $(- - -)$ for p = 0, $(-\square-)$ for p = 0.1%, and $(-\triangle-)$ for p = 0.5%. The figure shows: (a) the convergence of the objective function (12.2), (b) the numerical solutions for $\lambda(\theta)$ in comparison with the exact solution (**??**) shown with (——), and (c) the numerical solutions for $r(\theta)$ in comparison with the exact solution (11.7) shown with (——).

Table 3: Inverse problem III. The errors $E_\lambda = \|\underline{\lambda}_{exact} - \underline{\lambda}_{num}\|$ and $E_r = \|\underline{r}_{exact} - \underline{r}_{num}\|$ obtained without regularization for various percentages of noise p $\in \{0, 0.1, 0.5, 1\}$%.

	p	E_λ	E_r
linear boundary condition (3.1)	0	0.3816	0.1532
	0.1%	0.5875	0.1914
	0.5 %	1.8869	0.8297
	1 %	2.6569	1.0101
nonlinear boundary condition (4.1)	0	0.4570	0.1653
	0.1 %	0.6374	0.1876
	0.5 %	0.7667	0.2192
	1 %	0.7230	0.2881

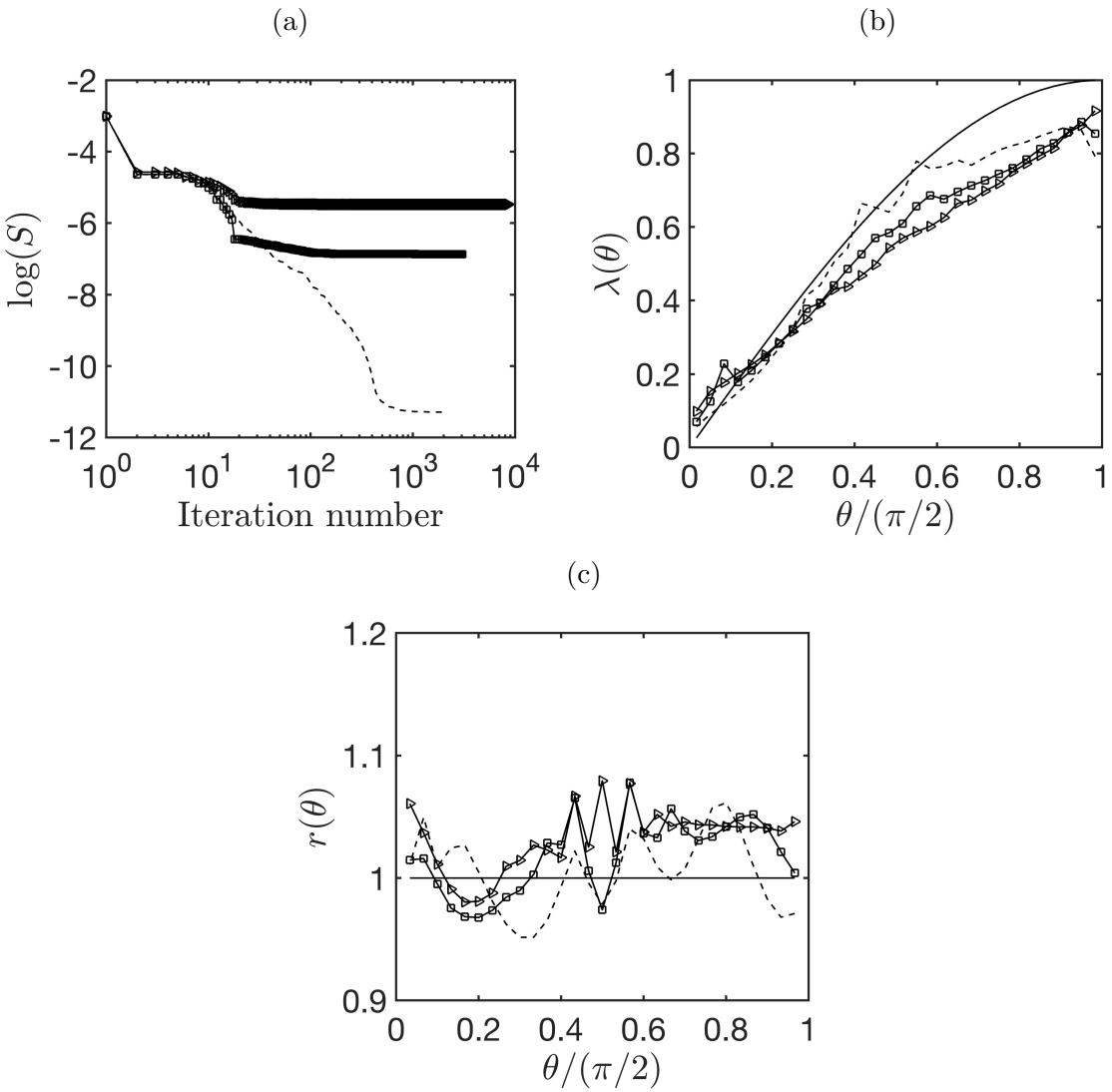

Figure 14: Inverse problem III. Numerical results obtained without regularization for the nonlinear boundary condition (4.1) for different noise levels: $(- - -)$ for p = 0, $(-\square-)$ for p = 0.1%, and $(-\triangle-)$ for p = 0.5%. The figure shows: (a) the convergence of the objective function (12.2), (b) the numerical solutions for $\lambda(\theta)$ in comparison with the exact solution (**??**) shown with (——), and (c) the numerical solutions for $r(\theta)$ in comparison with the exact solution (11.7) shown with (——).

sections 10 and 11, respectively. For full computational reproducibility and replicability purposes, the numerical code is shared in the Appendix.

In Figures 13 and 14, we present the numerical results for the linear boundary condition (3.1) and the nonlinear boundary condition (4.1), respectively, obtained by minimizing the unregularized least-squares functional (12.2) subject to the simple bounds on the variables (12.3) starting from the initial guess (12.4). Figures 13(a) and 14(a) illustrate the convergence behaviour of the constrained minimization, which is achieved in a few hundred iterations. Figures 13(b) and 14(b), and 13(c) and 14(c) illustrate the numerical reconstructions of the corrosion coefficient $\lambda(\theta)$ and of the polar radius $r(\theta)$ of the corroded boundary Γ_0. From Figures 13(b) and 13(c) it can be seen that instability sets in for the larger amount of noise of p = 0.5%, in case of the inverse problem III with the linear boundary condition (3.1). However, as also previously obtained in section 11.1 for the inverse problem II, the nonlinear boundary condition (4.1) seems to absorb some of the instability, as indicated in Figures 14(b) and 14(c), where the results obtained from inverting p = 0.5% noisy data are more stable than those recorded in Figures 13(b) and 13(c) for the linear boundary condition (3.1). The errors in the numerically obtained results for $\lambda(\theta)$ and $r(\theta)$ compared to their exact values (9.1) and (11.7) are given in Table 3. From this table, it can be seen that the errors decrease as the percentage of noise with which the input data (11.5) is contaminated decreases. Since the inverse problem III is a combination of the inverse problems I and II, it is interesting to compare the numerical results of Figures 13(c) and 14(c) shown with $(---)$ for the inverse problem III with those of Figures 7(b) and 9 shown with $(-\circ-)$ for the inverse problem II, for the linear and nonlinear boundary conditions (3.1) and (4.1), respectively. This comparison shows that, as expected, the retrievals for the polar radius $r(\theta)$ in the case of the inverse problem II are more accurate than those for the more complex combined inverse problem III.

12.1 Paremetrisation model reduction

Using regularization based on minimizing (12.1) instead of (12.2) did not show significant improvement and therefore those results are not presented. Instead, to improve the accuracy and stability of the numerical results, model reduction parametrisation can be employed by approximating the corrosion coefficient $\lambda(\theta)$ and the polar radius $r(\theta)$ using finite-dimensional trigonometric polynomials as [37, 81],

$$\lambda(\theta) = a_0 + \sum_{k=1}^{K} \left[a_k \cos(k\theta) + b_k \sin(k\theta)\right],$$

$$r(\theta) = c_0 + \sum_{k=1}^{K} \left[c_k \cos(k\theta) + d_k \sin(k\theta)\right], \quad \theta \in \left[0, \frac{\pi}{2}\right], \tag{12.5}$$

where $\underline{a} = (a_k)_{k=\overline{0,K}}$, $\underline{b} = (b_k)_{k=\overline{1,K}}$, $\underline{c} = (c_k)_{k=\overline{0,K}}$ and $\underline{d} = (d_k)_{k=\overline{1,K}}$ are unknown real coefficients to be determined. Alternatively, one could use cubic B-splines [60] in place of the trigonometric polynomial approximations (12.5). With the approximation (12.5), the objective functional (12.2), which previously consisted of estimating $2N-1$ variables $\underline{\lambda}$ and $\underline{r}$, now recasts in the form

$$S(\underline{a}, \underline{b}, \underline{c}, \underline{d}) = \frac{2}{2N} \sum_{j=2N+1}^{4N} \left(u_j^{(i)}(\underline{a}, \underline{b}, \underline{c}, \underline{d}) - h_j^{(i)}\right)^2, \tag{12.6}$$

Table 4: Inverse problem III. The errors $E_\lambda = \|\underline{\lambda}_{exact} - \underline{\lambda}_{num}\|$ and $E_r = \|\underline{r}_{exact} - \underline{r}_{num}\|$ in case of model reduction (12.5) with $K = 1$. These errors have been calculated at the same points $(\tilde{\theta}_i)_{i=\overline{1,N}}$ for $\underline{\lambda}$ and $(\theta_i)_{i=\overline{1,N-1}}$ for $\underline{r}$, as those used in Table 3.

	p	E_λ	E_r
linear boundary condition (3.1)	0	0.2771	0.1046
	0.5 %	0.3758	0.1552
	1 %	0.6750	0.2740
nonlinear boundary condition (4.1)	0	0.1222	0.0259
	0.5 %	0.3611	0.1498
	1 %	0.7311	0.2941

which requires estimating a reduced finite number of $4K + 2$ coefficients $\underline{a}$, $\underline{b}$, $\underline{c}$ and $\underline{d}$.

As we are trying to retrieve the circular boundary (11.7) and the sine function (9.1), the exact values of the coefficients in (12.5) are:

$$a_k^{exact} = 0,\ k = \overline{0, K}, \quad b_1^{exact} = 1, \quad b_k^{exact} = 0,\ k = \overline{2, K}, \tag{12.7}$$

$$c_0^{exact} = 1, \quad c_k^{exact} = d_k^{exact} = 0,\ k = \overline{1, K}. \tag{12.8}$$

We take $K = 1$, the lower and upper bounds on the variables

$$\begin{aligned} &0 \le a_0 \le 1, \quad -1 \le a_1 \le 1, \quad -1 \le b_1 \le 1.5, \\ &0.5 \le c_0 \le 1.5, \quad -0.5 \le c_1 \le 0.5, \quad -0.5 \le d_1 \le 0.5, \end{aligned} \tag{12.9}$$

and the initial guess

$$\left(a_0^{(0)}, a_1^{(0)}, b_1^{(0)}, c_0^{(0)}, c_1^{(0)}, d_1^{(0)}\right) = (0, 0, 0.5, 1.1, 0, 0)\,. \tag{12.10}$$

The minimization of the objective function (12.6) subject to the bounds (12.9) on the six variables a_0, a_1, b_1, c_0, c_1 and d_1 is performed using `lsqnonlin` starting from the initial guess (12.10). The numerically obtained results presented in Figures 15 and 16 and Table 4 show that the model reduction based on the approximations (12.5) with $K = 1$, significantly improves the computational efficiency, accuracy and stability of the numerical results, previously represented in Figures 13 and 14 and Table 3. Unlike the full model based on minimizing (12.2) in $2N-1 = 59$ unknowns, the reduced model based on minimizing (12.6) in $4K+2 = 6$ unknowns acts as an effective implicit regularization, preventing the appearance of spurious oscillation and providing smooth stable solutions. For larger values of K in (12.5), the least-squares functional (12.6) may need to be regularized in order to achieve stable solutions.

13 Conclusions and final remarks

This study has undertaken a thorough development of the BEM for solving three inverse problems concerned with the determination of boundary corrosion characteristics from one or two pairs of Cauchy data measurements taken on the outer accessible boundary of the ground within which a corroded pipe is buried. A peculiarity of corrosion modelling is that the linear or nonlinear boundary condition on the corroded boundary is of Robin type. The inverse boundary value problems for the Laplace's equation governing the

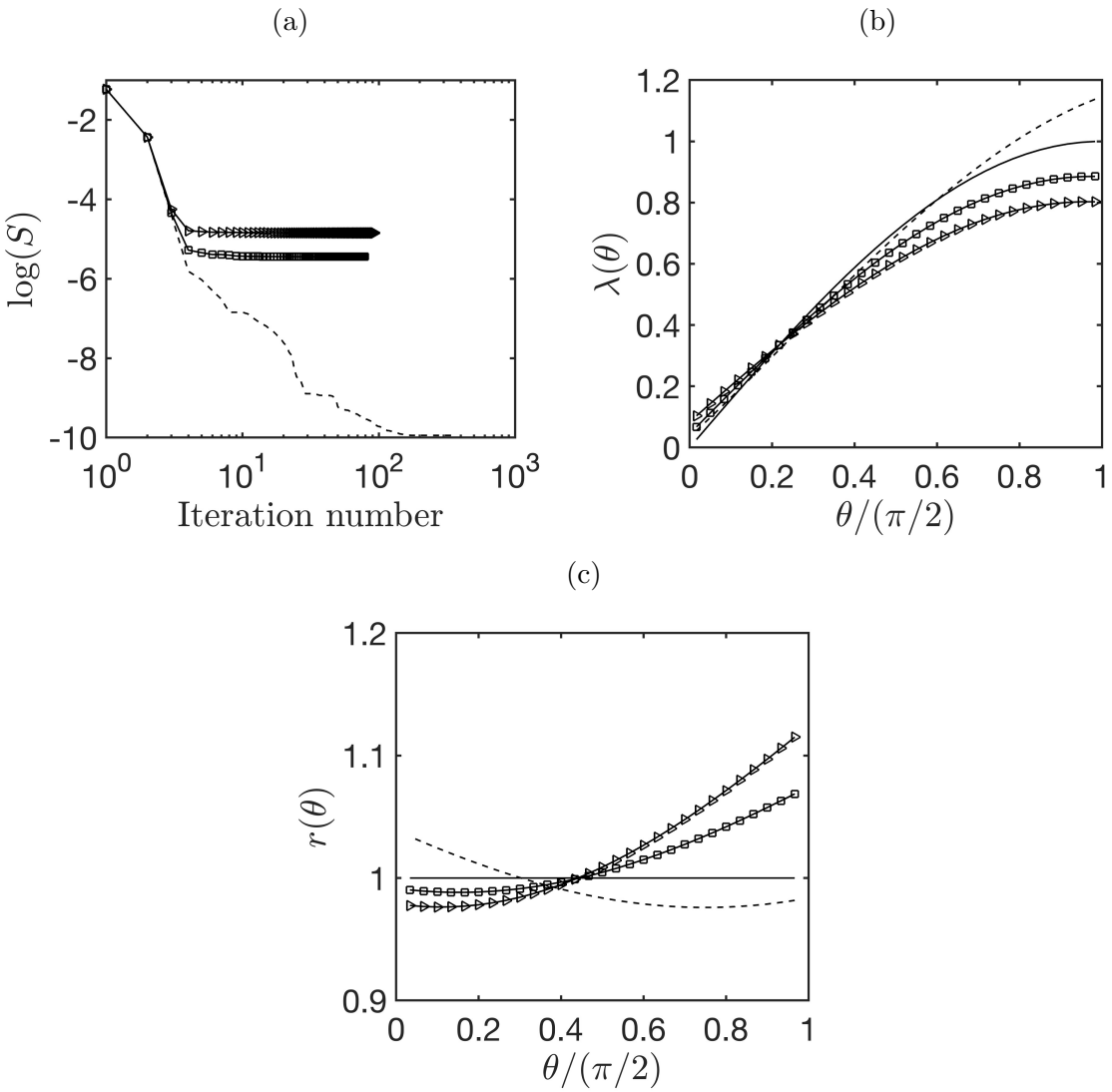

Figure 15: Inverse problem III. Numerical results obtained for the linear boundary condition (3.1) for different noise levels: $(- - -)$ for p = 0, $(-\square-)$ for p = 0.1%, and $(-\triangle-)$ for p = 0.5%, in case of model reduction (12.5) with $K = 1$. The figure shows: (a) the convergence of the objective function (12.6), (b) the numerical solutions for $\lambda(\theta)$ in comparison with the exact solution (**??**) shown with (——), and (c) the numerical solutions for $r(\theta)$ in comparison with the exact solution (11.7) shown with (——).

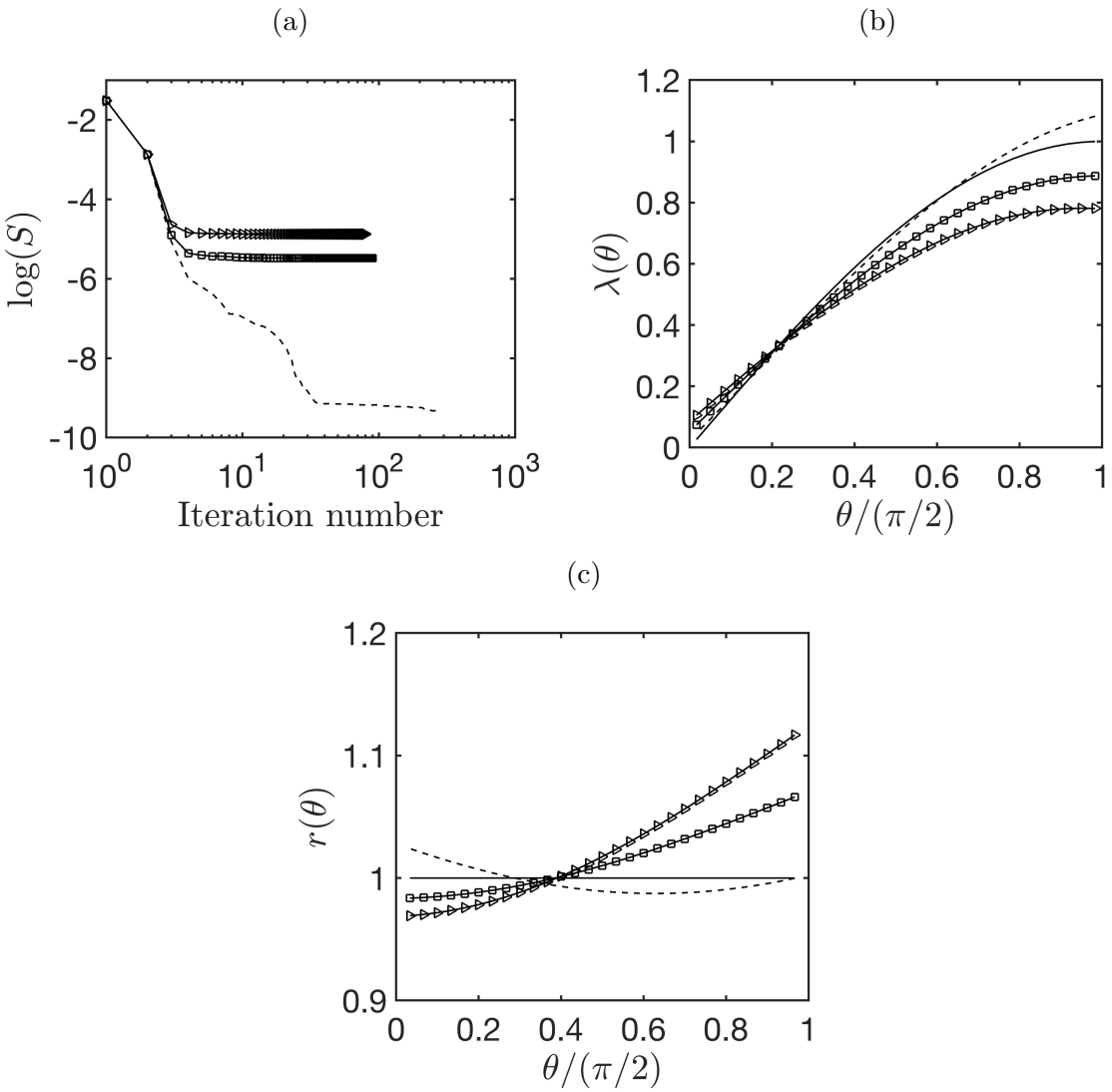

Figure 16: Inverse problem III. Numerical results obtained for the nonlinear boundary condition (4.1) for different noise levels: $(- - -)$ for p = 0, $(-\square-)$ for p = 0.1%, and $(-\triangle-)$ for p = 0.5%, in case of model reduction (12.5) with $K = 1$. The figure shows: (a) the convergence of the objective function (12.6), (b) the numerical solutions for $\lambda(\theta)$ in comparison with the exact solution (**??**) shown with (——), and (c) the numerical solutions for $r(\theta)$ in comparison with the exact solution (11.7) shown with (——).

electrical potential field have been recast in terms of nonlinear boundary integrals, and solved as constrained minimizations using the `lsqnonlin` Matlab toolbox optimization routine. Stability has been enhanced by penalising the nonlinear least-squares functionals involved using regularising terms imposing various orders of smoothness. Alternatively, the use of model reduction based on trigonometric polynomials stabilises the solutions of the studied inverse and ill-posed corrosion problems.

13.1 Insights and recommendations

• For the inverse problem I, the straightforward division (10.1) is not recommended; instead performing a constrained nonlinear inversion is more reliable.
• The inverse problems II and III require knowledge of at least two functionally independent Cauchy data. Moreover, model reduction parametrisation is recommended for practical purposes.
• The current hyperbolic sine (2.6) nonlinearity is rather weak to influence significantly the results in comparison with the linear law, but more testing needs to be done in the future for higher known or unknown nonlinear laws.
• The present study has ensured so far, the numerical verification of the boundary corrosion model based on the stable inversion of noisy simulated data; however, for model validation, raw experimental data need to be inverted in future investigations.

13.2 Extensions and limitations

Extensions of the BEM to anisotropic homogeneous [38], nonlinear [110] or with special spatial heterogeneity [19, 44, 50] materials are feasible. Of course, the BEM is limited to partial differential equations for which a fundamental solution is available in explicit form. Also, the nonlinear least-squares functional that was minimized requires a good initial guess due to its non-convex character, and using different objective functions [17, 89] may improve the convexity features.

More investigations into the robustness of reconstructions with respect to the initial guess and exploration of failure scenarios have been undertaken in the PhD thesis [8] of the first author. To our knowledge, a rigorous mathematical analysis into the uniqueness and stability of solution of the inverse problems I-III under general nonlinear corrosion laws is not available yet, but we hope that our numerical investigations have provided valuable insights into the ill-posedness of these problems.

13.3 Future work

Boundary conditions generalizing the Robin corrosion boundary condition (2.3) to include oblique derivative [24] or Laplacian [30, 31] terms will be considered with the BEM in future investigations. Future work may also consider extending the BEM developed in this study to solve inverse scattering problems governed by the Helmholtz equation in unbounded domains, exterior to an unknown obstacle whose boundary impedance and shape characteristics are to be detected from the measurement of the knowledge of the far field pattern of the scattered wave [65, 91, 109].

Acknowledgement

N.R. Altalhi expresses gratitude to the University of Leeds and Taif University for their support during her PhD studies at Leeds.

References

[1] M.T. Ahmed, J. Lavers and P. Burke (1989) An evaluation of the direct boundary element method and the method of fundamental solutions, *IEEE Transactions on Magnetics*, **25**, 3001–3006.

[2] G. Alessandrini, A. Morassi and E. Rosset (2002) Detecting cavities by electrostatic boundary measurements, *Inverse Problems*, **18**, 1333–1353.

[3] G. Alessandrini, L. Del Piero and L. Rondi (2003) Stable determination of corrosion by a single electrostatic boundary measurement, *Inverse Problems*, **19**, 973–984.

[4] G. Alessandrini and E. Sincich (2006) Detecting nonlinear corrosion by electrostatic measurements, *Applicable Analysis*, **85**, 107–128.

[5] G. Alessandrini and E. Sincich (2007) Solving elliptic Cauchy problem for identification of nonlinear corrosion, *Journal of computational and Applied Mathematics*, **198**, 307–320.

[6] N.R. Altalhi, D. Lesnic and S.D. Griffiths (2024) Solution of corrosion problems using the boundary element method, *WIT Transactions on Engineering Sciences*, **136**, 15–26.

[7] N.R. Altalhi, D. Lesnic and S.D. Griffiths (2025) Determination of a corroded boundary using the boundary element method, In: *Proceedings of the 14th UK conference on Boundary Integral Methods (UKBIM14)*, (ed. E. Chadwick), Salford University Press, Chapter **5**, pp. 36–48.

[8] N.R. Altalhi (2026) *Mathematical and Computer Modelling of Corrosion*, PhD Thesis, Department of Applied Mathematics, University of Leeds, UK.

[9] C.J.S. Alves and N.F.M. Martins (2008) Reconstruction of inclusions or cavities in potential problems using the MFS, In: *The Method of Fundamental Solutions – A Meshless Method*, (eds. C.S. Chen, A. Karageorghis and Y.S. Smyrlis), Dynamic Publishers Inc., Atlanta, pp. 51–73.

[10] H. Ammari, H. Kang, E. Kim, K. Louati and M.S. Vogelius (2008) A MUSIC-type algorithm for detecting internal corrosion from electrostatic boundary measurements, *Numerische Mathematik*, **108**, 501–528.

[11] H. Ammari, H. Kang and E. Kim (2009) Detection of internal corrosion, *ESAIM: Proceedings*, **26**, 207–216.

[12] H. Ammari, H. Kang, E. Kim, H. Lee and K. Louati (2009) Vibration testing for detecting internal corrosion, *Studies in Applied Mathematics*, **122**, 85–104.

[13] H. Ammari, H. Kang, E. Kim, M. Lim and K. Louati (2011) A direct algorithm for ultrasound imaging of internal corrosion, *SIAM Journal on Numerical Analysis*, **49**, 1177–1193.

[14] S. Aoki and Y. Urai (1992) Inverse analysis for estimating galvanic corrosion rate, In: *Inverse Problems in Engineering Mechanics*, (eds. M. Tanaka and H.D. Bui), Springer–Verlag, Berlin, pp. 547–556.

[15] S. Aoki, K. Amaya and M. Hayase (1994) Inverse analysis for improving accuracy of SVET in corrosion study, In: *Inverse Problems in Engineering Mechanics*, (eds. H.D. Bui, M. Tanaka, M. Bonnet, H. Maigre, E. Luzzato and M. Reynier), A.A. Balkema, Rotterdam, pp. 179–184.

[16] V. Bacchelli (2009) Uniqueness for the determination of unknown boundary and impedance with the homogeneous Robin condition, *Inverse Problems*, **25**, Article ID 015004, (4 pages).

[17] L. Beilina and M.V. Klibanov (2015) Globally strongly convex cost functional for a coefficient inverse problem, *Nonlinear Analysis: Real World Applications*, **22**, 272–288.

[18] E. Beretta and S. Vessella (1998) Stable determination of boundaries from Cauchy data, *SIAM Journal on Mathematical Analysis*, **30**, 220–232.

[19] J.R. Berger, P.A. Martin, V. Mantic and L.J. Gray (2005) The method of fundamental solutions for steady-state heat transfer in an exponentially graded material, *ZAMP*, **56**, 293–303.

[20] B. Bin-Mohsin and D. Lesnic (2012) Identification of a corroded boundary and its Robin coefficient, *East Asian Journal on Applied Mathematics*, **2**, 126–149.

[21] J.M. Birginie, F. Allard and A.J. Kassab (1996) Application of trigonometric boundary elements to heat and mass transfer problems, In: *BEM 18*, (eds. C.A. Brebbia, J.B. Martin, M.H. Aliabadi and N. Haie), WIT Press, Southampton, pp. 65–74.

[22] A. Bogomolny (1985) Fundamental solution method for elliptic boundary value problems, *SIAM Journal on Numerical Analysis*, **22**, 644–669.

[23] L. Bourgeois and J. Dardé (2010) A quasi-reversibility approach to solve the inverse obstacle problem, *Inverse Problems and Imaging*, **4**, 351–377.

[24] A. Bradji and D. Lesnic (2023) Steady-state inhomogeneous diffusion with generalized oblique boundary conditions, *ESAIM: Mathematical Modelling and Numerical Analysis*, **57**, 2701–2733.

[25] K. Bryan and M. Vogelius (2002) Singular solutions to a nonlinear elliptic boundary value problem originating from corrosion modeling, *Quarterly of Applied Mathematics*, **60**, 675–694.

[26] G. Burgess and E. Mahajerin (1984) A comparison of the boundary element and superposition methods, *Computers and Structures*, **19**, 697–703.

[27] B.M. Butler, A.J. Kassab, M.B. Chopra and V. Desai (1995) Galvanic corrosion predictions of roof systems at Walt Disney World, In: *Boundary Elements XVII*, (eds. C.A. Brebbia, S. Kim, T.A. Osswold and H. Power), Computational Mechanics Publications, Southampton, pp. 421–428.

[28] G. Buttazzo and R.V. Kohn (1987) Reinforcement by a thin layer with oscillating thickness, *Applied Mathematics and Optimization*, **16**, 247–261.

[29] F. Cakoni and R. Kress (2007) Integral equations for inverse problems in corrosion detection from partial Cauchy data, *Inverse Problems and Imaging*, **1**, 229–245.

[30] F. Cakoni and R. Kress (2013) Integral equation methods for the inverse obstacle problem with generalized impedance boundary condition, *Inverse Problems*, **29**, Article ID 015005, (19 pages).

[31] F. Cakoni, Y. Hu and R. Kress (2014) Simultaneous reconstruction of shape and generalized impedance functions in electrostatic imaging, *Inverse Problems*, **30**, Article ID 105009, (19 pages).

[32] S. Chaabane and M. Jaoua (1999) Recovering Robin's coefficients from boundary measurments, In: *Proceedings of 3ICIPE99, 1999 ASME Design Engineering Technical Conferences*, June 13–18, Port Ludlow, Washington, USA, (11 pages).

[33] S. Chaabane and M. Jaoua (1999) Identification of Robin coefficients by the means of boundary measurements, *Inverse Problems*, **15**, 1425–1438.

[34] S. Chaabane, I. Fellah, M. Jaoua and J. Leblond (2004) Logarithmic stability estimates for a Robin coefficient in two–dimensional Laplace inverse problems, *Inverse Problems*, **20**, 47–59.

[35] S. Chaabane, C. Elhechmi and M. Jaoua (2004) A stable recovery method for the Robin inverse problem, *Mathematics and Computers in Simulation*, **66**, 367–383.

[36] S. Chaabane, I. Feki and N. Mars (2012) Numerical reconstruction of a piecewise constant Robin parameter in the two- or three-dimensional case, *Inverse Problems*, **28**, Article ID 065016, (19 pages).

[37] K. Chaji, M. El Bagdouri and R. Channa (2008) A 2–D domain boundary estimation, *Journal of Physics: Conference Series*, **135**, Article ID 012029.

[38] Y.P. Chang, C.S. Kang and D.J. Chen (1973) The use of fundamental Green's functions for the solution of heat conduction in anisotropic media, *International Journal of Heat and Mass Transfer*, **16**, 1905–1918.

[39] R. Chapko and R. Kress (2005) A hybrid method for inverse boundary value problems in potential theory, *Journal of Inverse and Ill-Posed Problems*, **13**, 27–40.

[40] M. Charton, H.-J. Reinhardt and Dinh Nho Hao (2001) Numerical solution of a shape optimization problem, In: *Inverse Problems and Experimental Design in Thermal and Mechanical Engineering*, (eds. D. Petit, D.B. Ingham, Y. Jarny and F. Plourde), Proceedings of the Eurotherm Seminar **68**, pp. 101–107.

[41] C. Chen, H.A. Cho and M. Golberg (2006) Some comments on the ill–conditioning of the method of fundamental solutions, *Engineering Analysis with Boundary Elements*, **30**, 405–410.

[42] C. Chen, A. Karageorghis and Y. Li (2015) On choosing the location of the sources in the MFS, *Numerical Algorithms*, **72**, 107–130.

[43] C.S. Chen, A. Noorizadegan, D.L. Young and C.–S. Chen (2023) On the determination of locating the source points of the MFS using effective condition number, *Journal of Computational and Applied Mathematics*, **423**, Article ID 114955, (15 pages).

[44] A.H.–D. Cheng (1984) Darcy's flow with variable permeability: A boundary integral solution, *Water Resources Research*, **20**, 980–984.

[45] A.H.–D. Cheng, C.–S. Chen and A. Karageorghis (2025) *An Introduction to the Method of Fundamental Solutions*, World Scientific Publishing, Singapore.

[46] J. Cheng, Y.C. Hon and M. Yamamoto (2001) Conditional stability estimation for an inverse boundary problem with non–smooth boundary in $\mathbb{R}^3$, *Transactions of the American Mathematical Society*, **353**, 4123–4138.

[47] J. Cheng, M. Choulli and X. Yang (2006) An iterative BEM for the inverse problem of detecting corrosion in a pipe, In: *Frontiers and Prospects of Contemporary Applied Mathematics*, pp. 1–17.

[48] J. Cheng, M. Choulli and J. Lin (2008) Stable determination of a boundary coefficient in an elliptic equation, *Mathematical Models and Methods in Applied Sciences*, **18**, 107–123.

[49] M. Choulli (2004) An inverse problem in corrosion detection: stability estimates, *Journal of Inverse and Ill–Posed Problems*, **12**, 349–367.

[50] D.L. Clements (1980) A boundary integral equation method for the numerical solution of a second order elliptic equation with variable coefficients, *Journal of the Australian Mathematical Society, Series B*, **22**, 218–228.

[51] T.F. Coleman and Y. Li (1994) On the convergence of interior-reflective Newton methods for nonlinear minimization subject to bounds, *Mathematical Programming*, **67**, 189–224.

[52] T.F. Coleman and Y. Li (1996) An interior trust region approach for nonlinear minimization subject to bounds, *SIAM Journal on Optimization*, **6**, 418–445.

[53] W.B. da Silva, J.C.S. Dutra, C.E.P. Kopperschimidt, D. Lesnic and R.G. Aykroyd (2021) Sequential particle filter estimation of the time-dependent heat transfer coefficient in a multi-dimensional nonlinear inverse heat conduction problem, *Applied Mathematical Modelling*, **89**, 654–668.

[54] B.H. Dennis, G.S. Dulikravich and S. Yoshimura (2004) A finite element formulation for the determination of unknown boundary conditions for three-dimensional steady thermoelastic problems, *Journal of Heat Transfer*, **126**, 110–118.

[55] E. Divo, A.J. Kassab and F. Rodriguez (2004) An efficient singular superposition technique for cavity detection and shape optimization, *Numerical Heat Transfer, Part B*, **46**, 1–30.

[56] R. Duraiswami, G.L. Chahine and K. Sarkar (1997) Boundary element techniques for efficient 2-D and 3-D electrical impedance tomography, *Chemical Engineering Science*, **52**, 2185–2196.

[57] R. Duraiswami, K. Sarkar and G.L. Chahine (1998) Efficient 2D and 3D electrical impedance tomography using dual reciprocity boundary element techniques, *Engineering Analysis with Boundary Elements*, **22**, 13–31.

[58] T.E. Dyhoum, D. Lesnic and R.G. Aykroyd (2014) Solving the complete–electrode direct model of ERT using the boundary element method and the method of fundamental solutions, *Electronic Journal of Boundary Elements*, **12**, 26–71.

[59] M. Essahraoui, E. Cherrat, L. Afraites and J.F.T. Rabago (2025) Simultaneous recovery of corroded boundaries and admittance using the Kohn–Vogelius method, In: *International Conference on Mathematics Data Science*, (eds. A. Laghrib, M. Nachaoui and L. Afraites), Springer, Berlin, pp. 73–89.

[60] W. Fang and S. Zeng (2009) Numerical recovery of Robin boundary from boundary measurements for the Laplace equation, *Journal of Computational and Applied Mathematics*, **224**, 573–580.

[61] D. Fasino and G. Inglese (1999) An inverse Robin problem for Laplace's equation: theoretical results and numerical methods, *Inverse Problems*, **15**, 41–48.

[62] D. Fasino and G. Inglese (2001) Stability of the solutions of an inverse problem for Laplace's equation in a thin strip, *Numerical Functional Analysis and Optimization*, **22**, 549–560.

[63] D. Gilbard and N.S. Trudinger (1983) *Partial Differential Equations of Elliptic Type*, Springer, Berlin.

[64] P.C. Hansen (1992) Analysis of discrete ill-posed problems by means of the L-curve, *SIAM Review*, **34**, 561–580.

[65] L. He, S. Kindermann and M. Sini (2009) Reconstruction of shapes and impedance functions using few far-field measurements, *Journal of Computational Physics*, **228**, 717–730.

[66] G. Hu and M. Yamamoto (2015) Hölder stability estimate of Robin coefficient in corrosion detection with a single boundary measurement, *Inverse Problems*, **31**, Article ID 115009, (20 pages).

[67] C.–H. Huang and B.H. Chao (1997) An inverse geometry problem in identifying irregular boundary configurations, *International Journal of Heat and Mass Transfer*, **40**, 2045–2053.

[68] C.–H. Huang and T.–Y. Hsiung (1999) An inverse design problem of estimating optimal shape of cooling passages in turbine blades, *International Journal of Heat and Mass Transfer*, **42**, 4307–4319.

[69] C.–H. Huang and M.–T. Chaing (2009) A three-dimensional inverse geometry problem in identifying irregular boundary configurations, *International Journal of Thermal Sciences*, **48**, 502–513.

[70] T.M. Inc (2022) *Statistics and Machine Learning Toolbox*, Massachusetts, USA.

[71] G. Inglese (1997) An inverse problem in corrosion detection, *Inverse Problems*, **13**, 977–999.

[72] G. Inglese and F. Mariani (2004) Corrosion detection in conducting boundaries, *Inverse Problems*, **20**, 1207–1215.

[73] O. Ivanyshyn and R. Kress (2006) Nonlinear integral equations for solving inverse boundary value problems for inclusions and cracks, *Journal of Integral Equations and Applications*, **18**, 13–38.

[74] M. Jaoua, S. Chaabane, C. Elhechmi, J. Leblond, M. Mahjoub and J.R. Partington (2008) On some robust algorithms for the Robin inverse problem, *Revue Arima*, **9**, 287–307.

[75] B. Jin and J. Zou (2008) Inversion of Robin coefficient by a spectral stochastic finite element approach, *Journal of Computational Physics*, **227**, 3282–3306.

[76] B. Jin and J. Zou (2010) Numerical estimation of the Robin coefficient in a stationary diffusion equation, *IMA Journal of Numerical Analysis*, **30**, 677–701.

[77] R. Johnston and G. Fairweather (1984) The method of fundamental solutions for problems in potential flow, *Applied Mathematical Modelling*, **8**, 265–270.

[78] D.A. Jones (1996) *Principles and Prevention of Corrosion*, Prentice Hall, Upper Saddle River.

[79] J. Kaipio and E. Somersalo (2007) Statistical inverse problems: discretization, model reduction and inverse crimes, *Journal of Computational and Applied Mathematics*, **198**, 493–504.

[80] A. Karageorghis, D. Lesnic and L. Marin (2013) A moving pseudo-boundary MFS for three-dimensional void detection, *Advances in Applied Mathematics and Mechanics*, **5**, 510–527.

[81] A. Karageorghis, B. Bin-Mohsin, D. Lesnic and L. Marin (2015) Simultaneous numerical determination of a corroded boundary and its admittance, *Inverse Problems in Science and Engineering*, **23**, 1120–1137.

[82] A. Karageorghis, D. Lesnic and L. Marin (2023) An efficient moving pseudo-boundary MFS for void detection, *Engineering Analysis with Boundary Elements*, **147**, 90–111.

[83] A. Karageorghis, D. Lesnic and L. Marin (2024) Solution of inverse geometric problems using a non-iterative MFS, *Communications in Computational Physics*, **35**, 553–578.

[84] A.J. Kassab and J.E. Pollard (1993) Automated algorithm for the nondestructive detection of subsurface cavities by the IR-CAT method, *Journal of Nondestructive Evaluation*, **12**, 175–186.

[85] A.J. Kassab and J.E. Pollard (1994) Cubic spline anchored grid pattern algorithm for high-resolution detection of subsurface cavities by the IR-CAT method, *Numerical Heat Transfer, Part B*, **26**, 63–77.

[86] E. Katamine, H. Azegami and M. Kojima (2001) Boundary shape determination of steady-state heat-conduction fields, *Heat Transfer – Asian Research*, **30**, 245–258.

[87] P. Kaup and F. Santosa (1995) Nondestructive evaluation of corrosion damage using electrostatic boundary measurements, *Journal of Nondestructive Evaluation*, **14**, 127–136.

[88] P.G. Kaup, F. Santosa and M. Vogelius (1996) Method for imaging corrosion damage in thin plates from electrostatic data, *Inverse Problems*, **12**, 279–297.

[89] I. Knowles (1998) A variational algorithm for electrical impedance tomography, *Inverse Problems*, **14**, 1513–1525.

[90] R. Kress (2004) Inverse Dirichlet problem and conformal mapping, *Mathematics and Computers in Simulation*, **66**, 255–265.

[91] R. Kress and W. Rundell (2001) Inverse scattering for shape and impedance, *Inverse Problems*, **17**, 1075–1085.

[92] R. Kress and W. Rundell (2005) Nonlinear integral equations and the iterative solution for an inverse boundary value problem, *Inverse Problems*, **21**, 1207–1223.

[93] D. Lesnic, J.R. Berger and P.A. Martin (2002) A boundary element regularization method for the boundary determination in potential corrosion damage, *Inverse Problems in Science and Engineering*, **10**, 163–182.

[94] D. Lesnic (2021) *Inverse Problems with Applications in Science and Engineering*, Chapman and Hall/CRC.

[95] C.–S. Liu, C.–W. Chang and C.–Y. Chiang (2008) A regularized integral equation method for the inverse geometry heat conduction problem, *International Journal of Heat and Mass Transfer*, **51**, 5380–5388.

[96] J.–C. Liu and T. Wei (2010) Determination of a part of boundary for the Cauchy problem for the Laplace equation, *Inverse Problems in Science and Engineering*, **18**, 535–548.

[97] J. Liu and G. Nakamura (2017) Recovering the boundary corrosion from electrical potential distribution using partial boundary data, *Inverse Problems and Imaging*, **11**, 521–538.

[98] L. Marin, A. Karageorghis and D. Lesnic (2011) The MFS for numerical boundary identification in two-dimensional harmonic problems, *Engineering Analysis with Boundary Elements*, **35**, 342–354.

[99] N.S. Mera and D. Lesnic (2005) A three-dimensional boundary determination problem in potential corrosion damage, *Computational Mechanics*, **36**, 129–138.

[100] R.F. Millar (1970) The location of singularities of two–dimensional harmonic functions. I: Theory, *SIAM Journal on Mathematical Analysis*, **1**, 333–353.

[101] R. Nicholson and M. Niskanen (2021) Joint estimation of Robin coefficient and domain boundary for the Poisson problem, *Inverse Problems*, **38**, Article ID 015008.

[102] T.T.M. Onyango, D.B. Ingham and D. Lesnic (2009) Reconstruction of boundary condition laws in heat conduction using the boundary element method, In: *Seventh UK Conference on Boundary Integral Methods*, (eds. H. Power, A. La Rocca and S.J. Baxter), The University of Nottingham, pp. 87–98.

[103] C. Pagani and D. Pierotti (2009) Identifiability problems of defects with the Robin condition, *Inverse Problems*, **25**, Article ID 055007, (12 pages).

[104] A.G. Ramm (1986) A geometrical inverse problem, *Inverse Problems*, **2**, L19–L21.

[105] W. Rundell (2008) Recovering an obstacle and its impedance from Cauchy data, *Inverse Problems*, **24**, Article ID 045003, (22 pages).

[106] J.A.F. Santiago, J.C.F. Telles and W.J. Mansur (1992) Boundary element method in cathodic protection: simulation of polarization curves depending upon time and formation potential, In: *Boundary Elements XIV*, (eds. C.A. Brebbia, J. Dominguez and F. Paris), Vol. 1, Computational Mechanics Publications, Southampton, pp. 497–518.

[107] F. Santosa (1996) A level-set approach for inverse problems involving obstacles, *ESAIM: Control, Optimization and Calculus of Variations*, **1**, 17–33.

[108] F. Santosa, M. Vogelius and J.–M. Xu (1998) An effective nonlinear boundary condition for a corroding surface. Identification of the damage based on steady state electric data, *ZAMP*, **49**, 656–679.

[109] P. Serranho (2006) A hybrid method for inverse scattering for shape and impedance, *Inverse Problems*, **22**, 663–680.

[110] R.P. Shaw (1999) Steady-state heat conduction with separable position and temperature dependent conductivity, *Boundary Element Communications*, **10**, 15–18.

[111] E. Sincich (2007) Lipschitz stability for the inverse Robin problem, *Inverse Problems*, **23**, 1311–1326.

[112] M. Slodička and R. Van Keer (2004) A numerical approach for the determination of a missing boundary data in elliptic problems, *Applied Mathematics and Computation*, **147**, 569–580.

[113] K. Sorli and I.M. Skaar (2000) Monitoring the wear-line of a melting furnace, In: *1999 Inverse Problems in Engineering: Theory and Practice*, (ed. K.A. Woodburg), ASME, New York, pp. 271–281.

[114] Y. Tan (2009) Monitoring the corrosion of the blast furnace by perturbation method, *Series in Contemporary Applied Mathematics CAM*, **10**, 112–128.

[115] M.F. Valle, M.J. Colaço and F.S. Neto (2008) Estimation of the heat transfer coefficient by means of the method of fundamental solutions, *Inverse Problems in Science and Engineering*, **16**, 777–795.

[116] M. Vogelius and J.–M. Xu (1998) A nonlinear elliptic boundary value problem related to corrosion modeling, *Quarterly of Applied Mathematics*, **56**, 479–505.

[117] L.C. Wrobel and P. Miltiadou (2004) Genetic algorithms for inverse cathodic protection problems, *Engineering Analysis with Boundary Elements*, **28**, 267–277.

[118] W.– J. Yan and Y.–C. Ma (2006) The application of domain derivative for heat conduction with mixed condition in shape reconstruction, *Applied Mathematics and Computation*, **181**, 894–902.

[119] F. Yang, L. Yan and T. Wei (2009) Reconstruction of the corrosion boundary for the Laplace equation by using a boundary collocation method, *Mathematics and Computers in Simulation*, **79**, 2148–2156.

[120] F.L. Yang, L. Yan and T. Wei (2009) Reconstruction of part of a boundary for the Laplace equation by using a regularized method of fundamental solutions, *Inverse Problems in Science and Engineering*, **17**, 1113–1128.

[121] Y.–J. Yu and X.–L. Cheng (2017) Numerical identification of Robin coefficient by a Kohn–Vogelius type regularization method, *Inverse Problems in Science and Engineering*, **25**, 1014–1041.

Appendix

In this appendix, we present the MATLAB computational code based on the BEM and the toolbox routine `lsqnonlin` of minimization for the inverse problem III concerned with the simultaneous reconstruction of both the boundary geometry $r(\theta)$ and the corrosion coefficient $\lambda(\theta)$. The direct problem BEM solutions are computed using the `laplLBC_ID_Simu`, `laplLBC_Cnvx_Simu` and `laplNLBC_ID_Simu`, `laplNLBC_Cnvx_Simu` subroutines (not supplied herein, but available in [8]) for the linear (3.1) and nonlinear (4.1) boundary conditions, and the discontinuous (8.1) and continuous flux (8.2) inputs, respectively.

The implementation first generates the measurement data by solving direct problems with $N = 90$ for both flux scenarios, producing $h^{(1)}$ and $h^{(2)}$ on Γ_2 with noise added. For the inverse problem, $N = 30$ is used with the combined parameter vector $\underline{x} = [\underline{r}, \underline{\lambda}]^{\mathrm{T}}$ containing $\overline{1, N-1}$ radius values and $\overline{N, 2N-1}$ boundary corrosion coefficients. The initial guesses (12.4) are combined into the initial vector `x0 = [r_0,lambda_0]`. Box

constraints are defined separately for each parameter type with bounds $[0.5, 1.5]$ for r and $[0, 1]$ for λ, which are then combined into the vectors `lb = [R_law,lambda_law]` and `ub = [R_up,lambda_up]` of lower and upper bounds, respectively.

The objective function (12.1) of inverse problem III extends the formulations of the individual inverse problems I and II by combining the residuals from two measurements with regularization terms for both unknowns. The first-order derivative regularization term diff(λ) is computed using forward finite differences. At each iteration of the current estimates of r and λ, `lsqnonlin` calls both (for the fluxes g_1 and g_2) direct solvers to compute the corresponding solutions $u^{(1)}$ and $u^{(2)}$ on Γ_2 and compare them with the measured data $h^{(1)}$ and $h^{(2)}$. The `output` function tracks the convergence of the objective functional throughout the iterative minimization process.

```
clear;
clearvars -global;
addpath('../functions/')
global N X Y Z1 Z2 u  mu du  alpha beta h_S1 h_S2  mu_r mu_L R
global logobj_res li Ri lambda_0 R_0 x0  combined_norm reg_norm

% Parameters
p=0;
mu_r=0;
mu_L=0;
alpha=1;
beta=1;

% solve the direct with N=90
N=90;
M=7*N;
[X, Y, Z1, Z2] =SetGeo(N);
theta=(pi/2)*(1-((1:N)/N)+(1/(2*N)))';
R=ones(N-1,1);
lambda=sin(theta);

% direct solution
[u90_S1, du90_S1] = laplLBC_ID_Simu(N, R, X, Y, Z1, Z2, lambda);
[u90_S2, du90_S2] = laplLBC_Cnvx_Simu(N, R, X, Y, Z1, Z2, lambda);

% solve the Inverse problem with N=30
N=30;
M=7*N;
[X, Y, Z1, Z2] =SetGeo(N);
R=ones(N-1,1);
theta = (pi/2)*(1-(1:N)/N+(1/(2*N)))';
lambda=sin(theta);

% take h(s) on Gamma_1 from direct solution
rng('default');
rng(1);
h_S1 = u90_S1((2*90+2):3:(4*90));
h_S1 = h_S1 + h_S1 .* (p / 100) * (2 * rand(2*N,1) - 1);

h_S2 = u90_S2((2*90+2):3:(4*90));
h_S2 = h_S2 + h_S2 .* (p / 100) * (2 * rand(2*N,1) - 1);

% Initial guesses
```

```
R_0 = 1.1*ones(N-1,1);
lambda_0 = theta/(pi/2);
x0 = [R_0;lambda_0];        % Combined vectors

% lawer and upper Bounds for lambda and R
R_law = 0.5*ones(N-1,1);
R_up = 1.5*ones(N-1,1);
lambda_law = 0*ones(N,1);
lambda_up = 1*ones(N,1);

% Combined vectors of lawer and upper Bounds
lb = [R_law;lambda_law];
ub = [ R_up;lambda_up];

options = optimoptions('lsqnonlin','Display', 'iter','MaxIterations',
    10000, ...
     'MaxFunctionEvaluations', 1000000, 'FunctionTolerance', 1e-20, ...
     'StepTolerance', 1e-20,'OptimalityTolerance', 1e-15, 'OutputFcn',
    @outfun);
[x_res, resnorm, residual, exitflag, output] = lsqnonlin(
    @combinedObjective, x0, lb, ub, options);

% To Extract results
R_res = x_res(1:N-1);
lambda_res = x_res(N:end);

% save data
filename=['./data/inverseRecons_LBC_alpha',num2str(alpha),'_beta',
    num2str(beta),'_p',num2str(p),'_mu_r',num2str(mu_r),'_mu_L',num2str(
    mu_L),'.mat'];
save(filename,'x_res','logobj_res','p','mu','mu_r','mu_L','N','X','Y','
    R','lambda','h_S1','h_S2','u','du','combined_norm','reg_norm')

% Combined objective functions S = S1 + S2
function [fv] = combinedObjective(x)
     global combined_norm reg_norm alpha beta mu_r mu_L R_0 R lambda
    lambda_0 mu x_0
     fv_S1 = flsq_S1(x);
     fv_S2 = flsq_S2(x);
     fv = [alpha*fv_S1; beta*fv_S2; [mu_r * (R-R_0); mu_L * diff(lambda)
    ]];
     combined_norm=norm([alpha*fv_S1; beta*fv_S2]);
     reg_norm=norm([mu_r * (R-R_0); mu_L * diff(lambda)]);
end

% Objective function for S1 (Discontinuous flux)
function [fv_S1] = flsq_S1(x)
     global N h_S1 X Y Z1 Z2 u lambda  du
     R = x(1:N-1);
     lambda = x(N:end);
     [u,du] = laplLBC_ID_Simu(N, R, X, Y, Z1, Z2, lambda);
     fv_S1 = (2/(2*N)) * (u(2*N+1:4*N) - h_S1);
end

% Objective function for S2 (Continuous flux)
function [fv_S2] = flsq_S2(x)
     global N h_S2 X Y Z1 Z2 u lambda  du
     R = x(1:N-1);
```

```
    lambda = x(N:end);
    [u, du] = laplLBC_Cnvx_Simu(N, R, X, Y, Z1, Z2, lambda);
    fv_S2 = (2/(2*N)) * (u(2*N+1:4*N) - h_S2);
end

% Output function for logging
function stop = outfun(x, optimValues, state)
    stop = false;
    global logobj_res li Ri N
    i = optimValues.iteration;
    if  strcmp(state, 'iter') && i >= 0
        Ri(i+1, :) = x(1:N-1);
        li(i+1, :) = x(N:end);
        logobj_res(i+1) = log10(optimValues.resnorm);
    end
end
```